The Dissertation Committee for Kwok-Fan Chow certifies that this is the approved version of the following dissertation:

Development of Wireless DNA Microarray Sensors

Committee:

Richard M. Crooks, Supervisor

Allen J. Bard

Christopher Bielawski

Arumugam Manthiram

Keith Stevenson

Development of Wireless DNA Microarray Sensors

by

Kwok-Fan Chow, B.S.; M.S.

Dissertation

Presented to the Faculty of the Graduate School of
The University of Texas at Austin
in Partial Fulfillment
of the Requirements
for the Degree of

Doctor of Philosophy

The University of Texas at Austin
August, 2010

Dedication

To my wife,

Winnie

and my parents,

Yan-Ming and Kwai-Chun

Acknowledgements

I would like to sincerely thank my research advisor, Dr. Richard M. Crooks for his guidance and untiring support over the past five years. It has been my great privilege working in his laboratory. His encouragement was the most important factor leading to many fruitful developments.

I would also like to thank Dr. Allen J. Bard, Dr. Keith Stevenson, Dr. Christopher Bielawski, and Dr. Arumugam Manthiram for being my committee members and providing me with valuable suggestions throughout my graduate study.

My gratitude goes to Dr. François Mavré, Dr. Byoung-Yong Chang, and Mr. John A. Crooks for assisting me in this research. The many months we have spent together working in the laboratory and brainstorming at Starbucks have led to many important findings. Special thanks go to my fellow Crooks group members for their assistance in the laboratory.

Finally, I want to acknowledge and thank my lovely wife and parents for their undying support throughout my studies.

Development of Wireless DNA Microarray Sensors

Publication No._______________

Kwok-Fan Chow, Ph. D.
The University of Texas at Austin, 2010

Supervisor: Richard M. Crooks

The development of wireless DNA microelectrochemical microarray sensors is described. The operational principles of these sensors are based on bipolar electrochemistry. Bipolar electrodes are used to fabricate the wireless microarrays in this work. The systems are configured so that DNA sensing is carried out at the cathodic end of a bipolar electrode (BPE) and the result of the sensing experiment is reported at the anodic end of the BPE.

There are two types of reporting platforms developed in this study. The first type relies on the emission of electrogenerated chemiluminescence (ECL). The system is configured so that ECL is emitted at the anodic end of the

BPE when the target DNA is hybridized to the capture probe DNA immobilized on the cathodic end of the BPE. However, when there is no hybridization reaction occurs, there is no ECL emission on the electrode surface.

The second type of reporting platform developed is based on silver electrodissolution at the anodic end of a BPE. When a reduction reaction occurs at the cathodic end of a BPE, it triggers oxidation and dissolution of silver deposited at the anodic end of the BPE. The loss of silver can easily be detected by the naked eye. This detection principle is used for DNA detection: when the target DNA is hybridized to capture probe DNA on the BPE, the BPE becomes shorter. However, if target DNA does not hybridize to the electrode surface, the length of the BPE remains the same.

The BPE microarrays described in this work eliminate the need for complicated microfabrication procedures and instrumentation. For example, as many as 1000 BPEs can be simultaneously controlled using just two driving electrodes and a simple power supply. To fully utilize BPE microarrays for specific sensing tasks, a method based on robotic spotting was developed to modify the cathodic end of each BPE in the array. Because each BPE in a microarray is individually addressable, this development allows each BPE to perform a particular sensing operation.

Table of Contents

List of Tables

List of Figures

List of Schemes

Chapter 1: Introduction

1.1 Bipolar electrochemistry

A traditional three-electrode electrochemical cell is illustrated in Scheme 1.1a. It consists of a working electrode, an auxiliary electrode, and a reference electrode. In this configuration, the potential of the working electrode, which is related to the energy of the electrons in the electrode, is controlled (vs. a reference electrode) using a potentiostat. The potential of the solution is not directly controlled, or in other words it is at a floating potential. When the potential of the working electrode is set to a value more negative than that of an electroactive molecule in the solution, electrons may (depending upon kinetics) transfer across the electrode/solution interface (Scheme 1.1b). The rate of this electrochemical reaction is equivalent to the faradaic current measured in the circuit connecting the working and auxiliary electrodes. The key point is that the interfacial potential difference between the electrode and the solution, rather than the absolute potential of either of them, is the driving force for electron transfer.[1]

Scheme 1.1

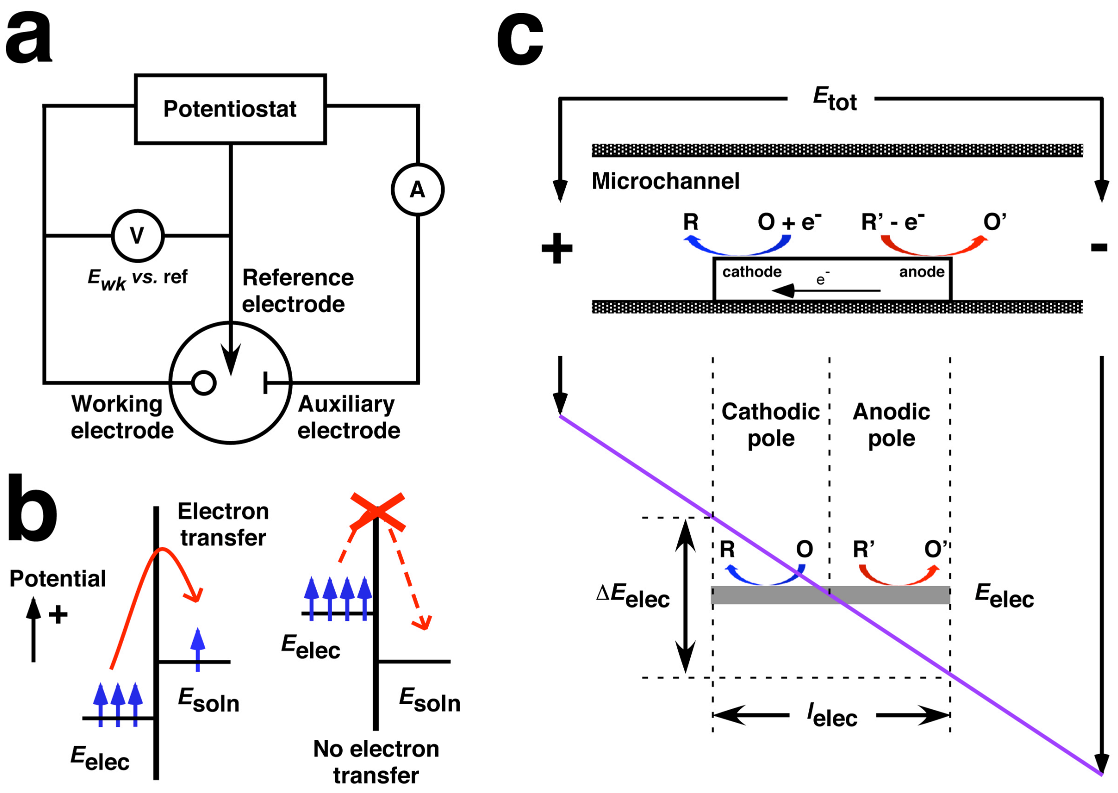
a
Potentiostat
A
V
E wk vs. ref
Reference electrode
Working electrode
Auxiliary electrode
b
Electron transfer
Potential
+
E elec
E soln
E elec
E soln
No electron transfer
c
E tot
Microchannel
+
-
R
O + e-
R' - e-
O'
cathode
e-
anode
Cathodic pole
Anodic pole
R
O
R'
O'
ΔE elec
E elec
l elec

The situation for a BPE is somewhat opposite to that of the conventional configuration; that is, for a BPE the potential of the solution is controlled while that of the BPE floats. The important point is that, despite the reversed roles of the solution and electrode in a BPE experiment versus a traditional three-electrode experiment, control is still maintained over the interfacial potential difference. The experimental configuration used to control BPEs is illustrated in Scheme 1.1c. A conductive material, which has no external electrical connection, is located inside a microchannel whose dimensions are generally small enough to ensure a high resistance to current flow. For example, in most of our experiments the channel is 1.2 cm long, 28 μm high, and 1.75 mm wide. The BPE itself is typically 0.5 – 1.0 mm in length. A simple power supply is used to apply a potential difference, E_{tot}, between two driving electrodes situated in reservoirs at both ends of the channel. Because the channel resistance is high, most of E_{tot} is dropped linearly along the channel length, and only a small fraction is lost at the driving electrode/solution interface (Scheme 1.1c).

To better understand how a BPE responds to E_{tot}, and how it interacts with the electrolyte solution in the microchannel, it is beneficial to describe an analogous electrical circuit comprised of parallel resistors (Scheme 1.2a and 1.2b). The total current in the channel (i_{channel}) can be carried either through the solution by ion migration (i_{s}) or through the electrode via electrons generated by faradaic processes at the BPE (i_{bpe}). The fraction of the current passing through the solution and the electrode depends on the relative values of R_{s}, which represents the resistance of the electrolyte solution, and R_{e}, which is the resistance of the BPE to faradaic electrochemistry, as given in eq 1.1.

$$\frac{i_{bpe}}{i_{channel}} = 1 - \frac{i_s}{i_{channel}} = \frac{R_s}{R_e + R_s} \qquad (1.1)$$

The potential difference between the solution and the two ends of the BPE (ΔE_{elec}, Scheme 1.1c), which is roughly a function of E_{tot} and the length of the electrode (l_{elec}), strongly influences R_{e}: a higher value of ΔE_{elec} results in a lower R_{e}. Likewise, eq 1.1 predicts that higher R_{s} results in more current passing through the BPE. At the extreme, when R_{s} approaches infinity, all of the channel current (i_{channel}) passes through the BPE.

Scheme 1.2

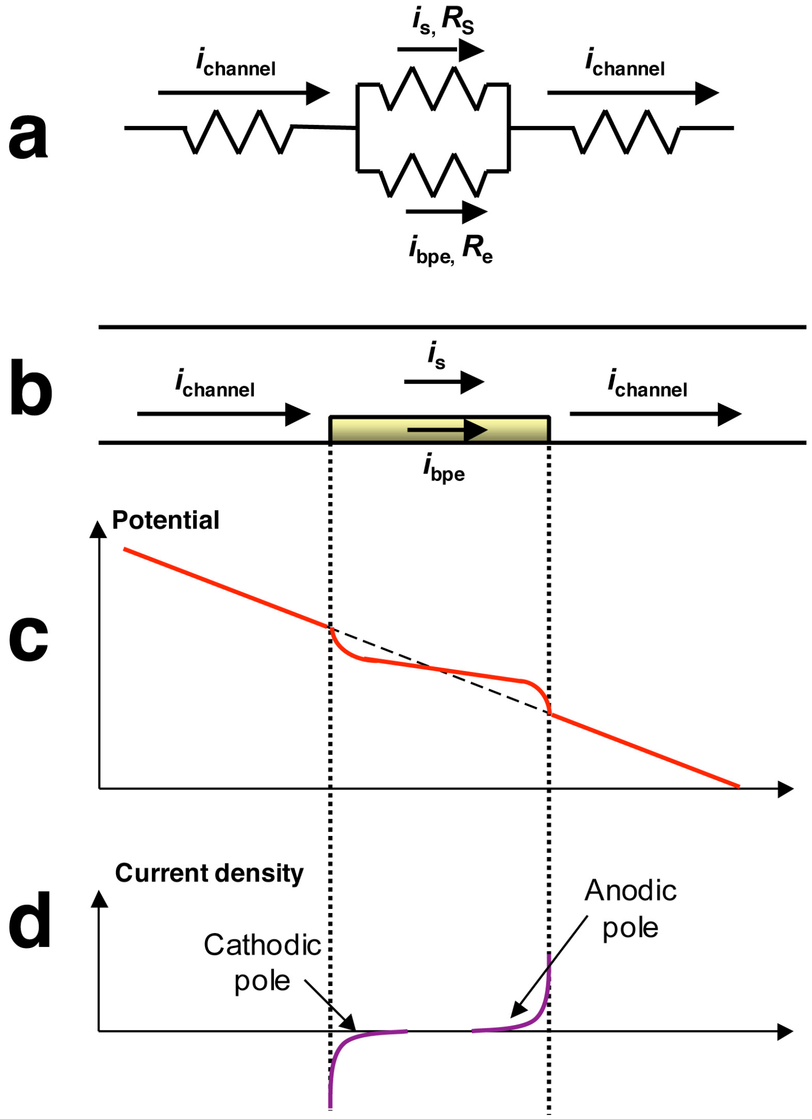

a
$i_{channel}$
i_s, R_S
$i_{channel}$
i_{bpe}, R_e
b
i_s
$i_{channel}$
$i_{channel}$
i_{bpe}
c
Potential
d
Current density
Anodic pole
Cathodic pole

Faradaic reactions at bipolar electrodes The bipolar effect can be understood more completely if one considers the variation of potential difference at the electrode/solution interface along the entire length of the electrode. Scheme 1.1c shows that a lateral potential drop in the electrolyte solution results in the potential of the electrode floating to an equilibrium value, E_{elec}, that separates the BPE into two poles: the cathodic pole, where the solution potential is higher than E_{elec}, and the anodic pole, where the solution potential is lower than E_{elec}. Accordingly, there is a potential difference at each lateral position of the electrode solution/interface that may or may not be sufficient to drive an electrochemical reaction. These cathodic and anodic electrochemical processes are coupled electrically via the electrode, and they must occur simultaneously and at the same rate to ensure that electroneutrality is maintained within the conductive BPE. This relationship means that the total current flowing through each pole of the BPE is the integrated sum of the current at every location in that pole (scheme 1.2d).

Excluding mass transfer effects, the current density at the BPE mainly depends on two parameters: the overpotential available at every location at the electrode/solution interface, and the kinetic characteristics of the redox couples involved in the faradaic processes. As mentioned earlier, ΔE_{elec} is the fraction of E_{tot} that is dropped across the BPE (Scheme 1.1c), and it represents the total driving force available to couple the two faradaic reactions at the poles of the BPE. For these two redox processes to occur simultaneously, the value of ΔE_{elec} has to be higher than the difference in the formal potentials for the two reactions.[2] The ΔE_{elec} available in the system can be approximated by eq 1.2.

$$\Delta E_{\mathrm{elec}} = \frac{E_{\mathrm{tot}}}{l_{\mathrm{channel}}} l_{\mathrm{elec}} \qquad (1.2)$$

It follows that for a given electric field ($\sim E_{\mathrm{tot}}/l_{\mathrm{channel}}$), longer electrodes yield a higher value of ΔE_{elec}, resulting in a larger value of i_{bpe}. Consequently, the value of E_{tot} required to induce faradaic reactions varies depending both on the species present in solution and on the ratio of electrode length to channel length (or, in other words, the slope of the purple line in Scheme 1.1c). For most of the results reported here, E_{tot} is in the range of 10-30 V, and it never exceeds 100 V. Therefore, inexpensive power supplies are sufficient to carry out many different kinds of interesting experiments with BPEs.

Background Although BPEs have not been widely adopted for electroanalytical purposes, they have been used for many years in battery technologies, for electrosynthesis,[3, 4] as photoelectrodes for solar cells,[5-7] and as seeds to generate nanowires along electric field lines.[8] More recently, Sen, Mallouk, and coworkers have shown that bipolar electrochemistry can lead to self-propulsion of freely suspended nanorods.[9] In this experiment, a bimetallic Pt/Au nanorod electrocatalyzes the oxidation and reduction of H_2O_2 at the Pt and Au sites, respectively, and this leads to predictable motion of the nanorods. Bipolar electrochemistry has also been used to prepare surfaces modified with gradients of various materials. This application relies on the axial gradient in the potential difference between the solution and BPE discussed earlier (Scheme 1.1c). Using this principle, molecular gradients of self-assembled monolayers have been prepared on Au surfaces,[10, 11] Au has been electrodeposited onto the ends of carbon nanotubes,[12] and graded compositions of CdS have been synthesized.[13]

1.2 Electrochemical DNA Microarrays

Microarrays are used to analyze small samples containing complex mixtures of many analytes. For instance, DNA microarrays can be used to analyze thousands of different types of DNA sequences in a single sample. The advantages of using electrochemical transducers to detect DNA hybridization are their high sensitivity, small dimensions, and compatibility with micro-manufacturing technologies.

Electrochemical sensing experiments are normally carried out in a two- or three-electrode cell configuration, and a single working electrode is used to detect the presence of a redox-active analyte of interest. The amount of current that passes between the counter and working electrodes is directly related to the concentration of the redox species. Because of the small size of electrochemical microarrays, they typically adopt a two-electrode design. A separate wire connection and a potentiostat are required to measure the current passing through these two electrodes. In an array composed of thousands of electrodes, the fabrication procedure gets very complicated, and the time necessary to measure the current through each electrode can be prohibitive. In the experiments discussed later, we developed an efficient way to fabricate a large-scale microelectrochemical DNA microarray sensors that overcome these deficiencies.

Like most DNA sensing methods, electrochemical detection usually requires a tag to directly or indirectly label the target DNA. For direct detection, the target DNA requires modification with the label. However, in a sandwich assay, there is no need to modify the target DNA. Once the target DNA is hybridized to the capture probe DNA on the electrode surface, another DNA sequence carrying the tag (reporting probe) is hybridized to the target. There are three main categories of commonly used tags: nanoparticles, enzymes, or electrochemical active molecules.[14] Electrochemical detection is based on the faradaic current resulting, either directly or indirectly, from the tag. All the DNA sensing experiments discussed in this work are based on direct labeling of the target DNA.

Pt is a very good electrocatalyst for the oxygen reduction reaction (ORR). Willner et al. have demonstrated that platinum nanoparticles (Pt-NPs) can be used to label the target DNA (Scheme 1.3a).[15] When the Pt-NP-modified DNA is hybridized to complementary DNA immobilized on a gold surface, a large ORR peak is observed at ~ -0.1 V vs.

Scheme 1.3

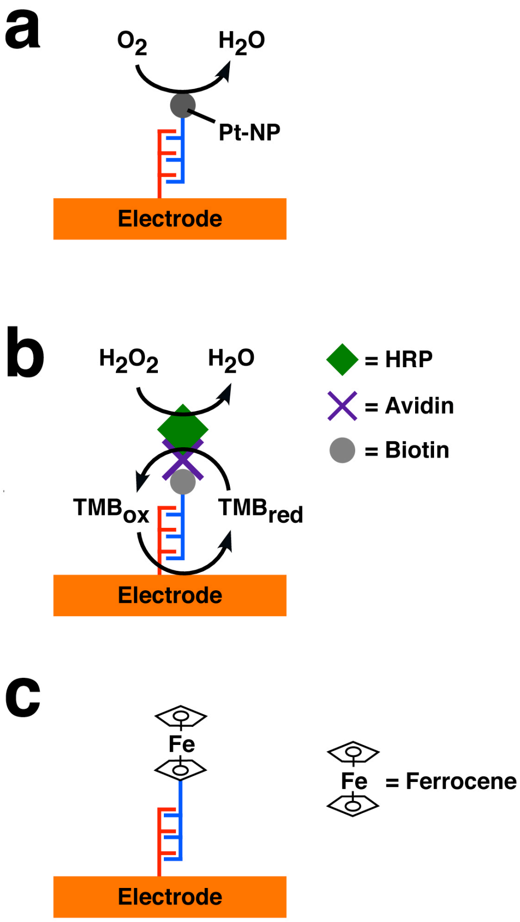
a
O_2
H_2O
Pt-NP
Electrode
b
H_2O_2
H_2O
= HRP
= Avidin
= Biotin
TMB_{ox}
TMB_{red}
Electrode
c
Fe
Fe
= Ferrocene
Electrode

Ag/AgCl. However, when Pt-NP labeled DNA is absent, no reduction peak is observed at this potential. Therefore, this labeling approach is able to report DNA hybridization.

An example of an enzymatic label is avidin conjugated horseradish peroxidase (HRP).[16] It binds to the biotin-modified target DNA after hybridization to the capture probe DNA on the electrode surface (Scheme 1.3b). A solution containing tetramethylbenzidine (TMB) and H_2O_2 is then introduced to the electrode surface for the enzymatic reactions. HRP catalyzes the reduction of H_2O_2 to H_2O while simultaneously oxidizing the reduced form of TMB (TMB_{red}) to the oxidized form (TMB_{ox}). Because TMB is an electrochemical active compound, TMB_{ox} can be reduced back to TMB_{red} on the electrode surface. The amount of enzyme is directly proportional to the amount of hybridized DNA, therefore the TMB reduction current can be correlated to the amount of target DNA.

For the electrochemical active molecule tagging, ferrocene (Fc) is often used in DNA biosensors and microarrays.[14] When the target DNA is labeled with Fc, it can be oxidized directly on the electrode surface (Scheme 1.3c). When an oxidizing potential is applied, the faradic current measured is directly related to the number of DNA sequences hybridized to the capture probe DNA.

In the DNA detection experiments discussed in the later chapters, Pt-NPs and avidin conjugated HRP were employed to label the target DNA.

1.3 Research Summary and Accomplishments

My dissertation focuses on the development of BPE microarrays for DNA sensing and as a tool for understanding fundamental properties of BPE. Two different DNA BPE sensing platforms have been developed in this study: ECL and Ag electrodissolution based BPE microarray sensors. The importance of the BPE microarrays developed in this study is that only two driving electrodes and a simple power supply are needed to operate an entire microarray. The unique nature of the BPE allows the sensing and reporting reactions to occur simultaneously at the two poles of the BPE. In contrast to the typical electrochemical microarrays, BPE microarrays do not require complicated wire connections to read out the state of each sensing electrode.

Chapters 3, 4, and 5 describe the sensing platforms based on the emission of ECL at the anodic end of the BPE to report the sensing event occurring at the cathodic end of the BPE. Specifically, chapter 3 discusses how a wireless microelectrochemical DNA microarray sensor is developed. The BPEs housed inside a microchannel are immobilized with capture probe DNA. When an electric field is applied across the microchannel, ECL is emitted only on the anodic end of the BPE if the platinum nanoparticle labeled complementary DNA is present on the cathodic end of the electrode surface.

Chapter 4 describes a large-scale BPE microarray composed of 1000 BPEs. A method of using a robotic spotter to immobilize DNA at the cathodic end of each BPE is also described. Because each BPE in the microarray is individually addressable, this development allows each BPE to perform a different sensing task. The experimental results shown in chapters 3 and 4 are backed with the theoretical study presented in chapter 5. In addition, split BPEs are designed to correlate the relationship between the current passing through the electrodes and the ECL intensity. The importance of this design is that it allows the determination of the sensitivity for BPE sensing.

Chapter 6 describes another DNA sensing platform based on electrodissolution of Ag at the anodic end of the BPE. When the target DNA binds to the capture probe at the cathodic pole of the BPE, it triggers the oxidation and electrodissolution of Ag metal present at the anodic pole. The significance of this experiment is that the loss of Ag is easily detectable with the naked eye or a magnifying glass and provides a permanent record of the electrochemical history of the electrode.

Chapter 2: Experimental

2.1 Chemicals

All chemicals used in this work are described in the individual chapters.

2.2 Techniques

Photolithography and soft lithography

Photolithography uses light to form a pattern on a substrate surface.[17] All of the bipolar electrodes used in this work were fabricated by contact-mode photolithography. In contact-mode photolithography, the photomask is in direct physical contact with the photoresist layer and a vacuum is used keep the two layers in close proximity, ~1 μm. The dimensions of the design on the photomask are transferred directly to a photoresist and the resolution is typically ranging from 0.5 to 0.8 μm.

To use contact-mode photolithography, a layer of photoresist is first spin-coated onto a gold slide (parts i and ii of Scheme 2.1a). A photomask containing the design of the BPEs is then placed on top of the gold slide under a mask aligner (part iii of Scheme 2.1a). UV light is passed through the photomask onto the photoresist layer. The BPE

Scheme 2.1

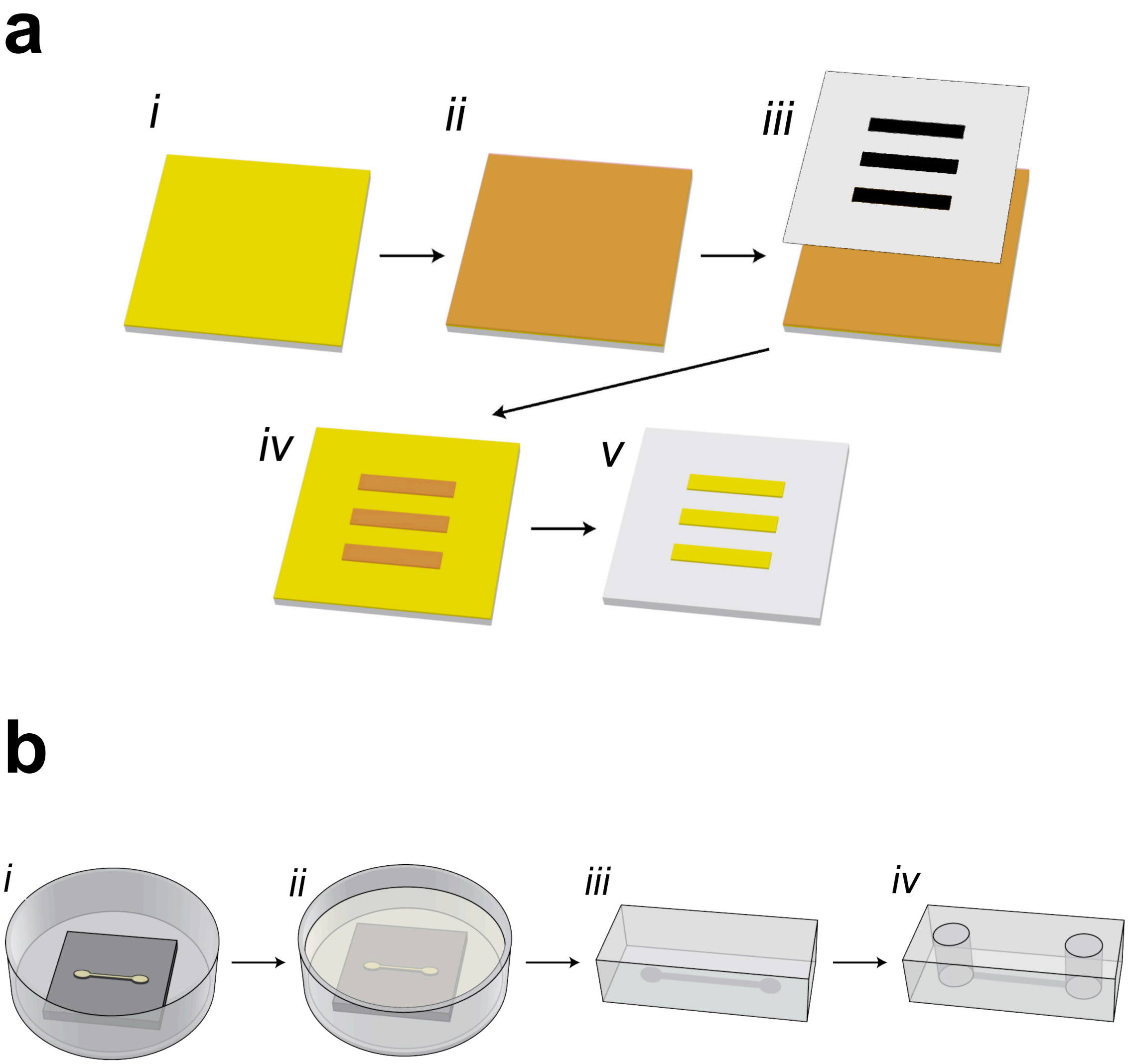

patterns are transferred to the Au slide after developing the photoresist and etching the Au and Cr adhesion layers (part iv of Scheme 2.1a).[18] The remaining photoresist is then removed by acetone (part v of Scheme 2.1a). The BPEs are ready to use directly or, for DNA immobilization (Chapters 3, 4, and 6), after cleaning with piranha (3:1 concentrated sulfuric acid to 30% hydrogen peroxide. Warning: Piranha solution is a strong oxidant and reacts violently with organic materials. It should be handled with extreme care and all work should be performed under a fume hood with protection gears.) Specific details about the fabrication procedures are provided in the experimental section of each chapter.

The microchannels used in this work (Chapters 3 and 5) were fabricated by using soft lithography.[17] The mold of the microchannel was a layer of photoresist coated on a glass slide fabricated by photolithography. In short, a layer of photoresist is spin-coated onto a glass slide surface. The patterns of the microchannel are then transferred to the photoresist (part i of scheme 2.1b). The height of the microchannel is controlled by the thickness of the photoresist layer. Once, the mold is silianized, it is ready for microchannel fabrication.

To form a glass-PDMS hybrid microchannel, the PDMS precursor is first poured onto the photoresist mold (part ii of Scheme 2.1b). After heat curing (~70 °C for 2 h), the PDMS can be peeled off from the mold (part iii of Scheme 2.1b). A hole puncher is used to form the reservoirs at the two ends of the microchannel (part iv of Scheme 2.1b). For reversible binding, the PDMS microchannel is simply placed on top of a glass surface. Binder clips are used to hold the microchannel in place. For irreversible binding, the PDMS and glass slide are first treated with an air plasma. After binding the PDMS and glass slide together, the device is heated at ~80 °C for 1 min.

Chapter 3: Wireless Electrochemical DNA Microarray Sensor

3.1 Synopsis

In this chapter we describe an electrochemical DNA microarray sensor whose function is controlled with just two wires regardless of the number of individual sensing electrodes. The bipolar sensing electrode is modified with probe DNA, and the anode end of each electrode is configured to emit light (electrogenerated chemiluminescence) upon hybridization of complementary DNA labeled with electrocatalytic (oxygen reduction) Pt nanoparticles at the cathode. The important finding is that DNA can be selectively detected at an array of three electrodes. In principle, however, this advance provides a means for controlling the potential of many electrodes using just two wires, and then indirectly determining the current flowing through all of them simultaneously by correlating light emission to current.

3.2 Introduction

In this chapter we report an electrochemical DNA microarray sensor whose function is controlled using just two wires regardless of the number of individual sensing electrodes. This advance is enabled by confining bipolar sensing electrodes within a microfluidic channel (part a of Scheme 3.1), and exerting potential control over the electrolyte solution rather than individual electrodes. In this configuration, the two driving electrodes control the potential difference between the sensing electrodes and the solution, and the current at the sensing electrodes is indirectly measured by taking advantage of electrogenerated chemiluminescence (ECL) present at the anode end of each bipolar electrode. This approach can be used to sense hybridization of DNA oligonucleotides.

Electrochemistry is normally carried out by controlling the electrode potential. However, because the potential difference between the electrode and the solution drives the electron-transfer reaction, it is equally effective to control the potential of the solution. Our approach for using this principle is illustrated in part b of Scheme 3.1.[19, 20] An external potential (E_{tot}) is applied to the two ends of a microchannel, and the resistance of the electrolyte solution results in a linear potential gradient ($\mathrm{d}E/\mathrm{d}x$) along the channel. The difference in potential between the two ends of the bipolar electrode (ΔE_{elec}) is the fraction of E_{tot} dropped across the length of

Scheme 3.1

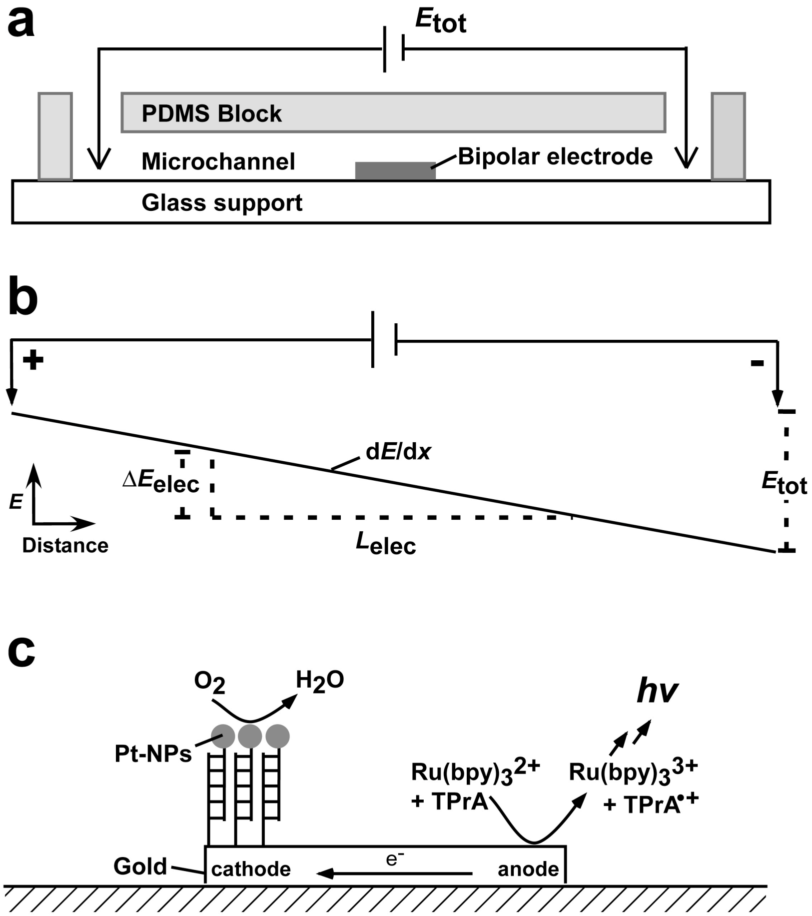

a
E_{tot}
PDMS Block
Microchannel
Bipolar electrode
Glass support
b
+
-
dE/dx
ΔE_{elec}
E
Distance
L_{elec}
E_{tot}
c
O_2
H_2O
hv
Pt-NPs
$Ru(bpy)_3^{2+}$
+ TPrA
$Ru(bpy)_3^{3+}$
+ $TPrA^{\bullet+}$
Gold
cathode
e^-
anode

this electrode (L_{elec}). If ΔE_{elec} is sufficiently large, then faradaic electrochemical processes will occur simultaneously at both ends of the bipolar electrode. Because of the requirement for charge balance, the rate of electron transfer (i.e., the current) at both ends of the electrode must be the same.

A significant deficiency of bipolar electrochemistry is that there is no convenient means for directly measuring current flowing within an electrode. The experimental configuration illustrated in part c of Scheme 3.1 addresses this problem. Here, E_{tot} is held at a sufficiently high value that the ECL reaction resulting from the oxidation of $Ru(bpy)_3^{2+}$ and tri-*n*-propylamine (TPrA),[21-23] indicated at the anode end of the bipolar electrode, is activated upon electrocatalytic reduction of O_2 at the cathode end of the electrode. In the sensing experiments discussed next, the oxygen reduction reaction (ORR) is catalyzed by hybridization of target DNA labeled with Pt nanoparticles (Pt-NPs) to previously immobilized capture DNA.[15] Accordingly, in the presence of DNA hybridization at the cathode, light is emitted from the anode.

3.3 Experimental

Chemicals, Materials, Characterization Gold-coated slides (EMF, Ithaca, NY) were used to fabricate the bipolar electrodes. The poly(dimethylsiloxane) (PDMS) microfluidic channel was prepared from Sylgard 184 (Dow Corning, Midland, MI). The platinum salt, H_2PtCl_6, used for Pt-NP synthesis was obtained from Strem Chemicals, Inc. The following chemicals were purchased from Sigma-Aldrich: 6-Mercapto-1-hexanol (63762), $Ru(bpy)_3Cl_2 \bullet 6H_2O$ (bpy = 2,2′-bipyridine) (224758), and tri-*n*-propylamine (239712).

All DNA oligonucleotides were synthesized and purified (HPLC) by Integrated DNA Technologies (Coralville, IA) and used without further purification. The sequences and modifications are as follows: capture probe, (5′-CAC GAC GTT GTA AAA CGA CGG CCA G-$(CH_2)_6$ SH-3′); target, (5′-CTG GCC GTC GTT TTA CAA CGT CGT G-$(CH_2)_6$ SH-3′).

A microscope (Nikon AZ100, Nikon Co., Tokyo, Japan) equipped with a CCD camera (Cascade, Photometrics Ltd., Tucson, AZ) was used to obtain the optical and luminescence micrographs. Micrographs were proceed using V++ Precision Digital Imaging software (Digital Optics, Auckland, New Zealand).

Synthesis of platinum nanoparticles The synthesis of the platinum nanoparticles was inspired by a previously reported procedure.[24] It is based on the chemical reduction of a platinum salt by a strong reducing agent, and the use of citrate ions as stabilizers. Briefly, 15.0 mL of a 500.0 μM H_2PtCl_6 aqueous solution was mixed with 1.00 mL of a 50.0 mM sodium citrate solution in a glass vial. Next, 0.500 mL of a 30.0 mM $NaBH_4$ solution was added drop wise with a pipette in 5 μL steps. The vial was sealed and the solution was stirred for 30 min.

Characterization of platinum nanoparticles Transmission electron micrographs (TEM) were obtained using a JEOL-2010F TEM operating at 200 kV. The sample grids for imaging were prepared by dropping 8 μL of the sample onto a carbon-coated copper grid (EM Sciences, Gibbstown, NJ) followed by solvent evaporation in air at room temperature. Part a of Figure 3.1 shows that the nanoparticles are roughly spherical in shape. The size distribution (part b of Figure 3.1) was determined using Sigma scan software: the measured average size is 3.9 ± 0.8 nm.

Surface modification of bipolar electrodes The bipolar electrodes were fabricated by using a standard micromolding method. Prior to electrode modification, the

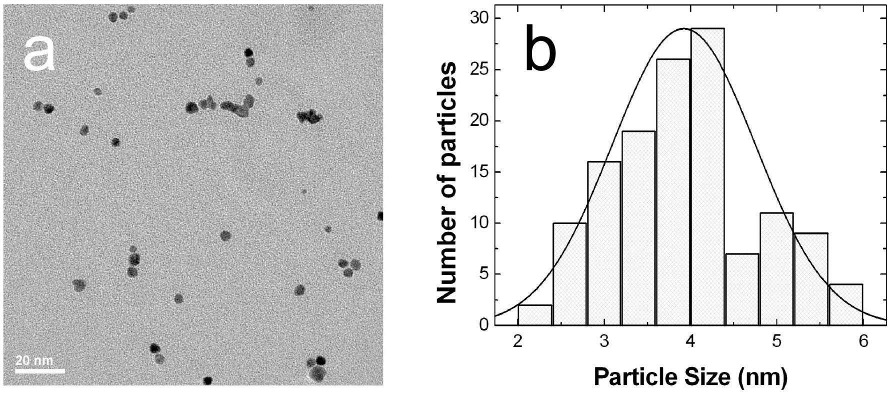

Figure 3.1. (a) TEM image of the Pt-NPs. (b) Size distribution histogram of the Pt-NPs.

microfabricated gold slide was cleaned in a piranha solution for 10 min (Warning: Piranha solution is a strong oxidant and reacts violently with organic materials. It should be handled with extreme care and all work should be performed under a fume hood with protection gears.) The entire surface of each gold, bipolar electrode was modified with single-strand DNA (ssDNA) capture probes by placing 15 μL of the thiol-functionalized DNA solution (2.5 μM in TE buffer containing 10.0 mM Tris, 1.00 mM EDTA, and 0.10 M NaCl, pH 7.4) on the electrode surfaces. The solution remained in contact with the electrode for 2 h in a sealed humidity chamber at 20-25 $^{\circ}$C. The same DNA modification procedure was carried out on a macroscopic disk gold electrode, and the surface coverage of the DNA probe was found to be 2.1×10^{-12} mol/cm^2 by a previously reported procedure.[25] Next, the electrodes were rinsed with a TE buffer solution to remove excess DNA solution. All the rinsing was done using a wash bottle containing a TE buffer solution to wash the electrodes surface for a min. A 6-mercaptohexanol solution (1 μM in 1 vol% ethanol in water) was then brought into contact with the electrode surfaces for 1 h to back-fill vacancies within the DNA submonolayer.

TE buffer was used to remove excess thiol solution, and then the electrodes were ready for experiments.

Target DNA labeled with Pt NPs was prepared by mixing a 25:1 molar ratio of DNA:Pt-NPs for 30 min. This solution was placed onto the probe-modified bipolar electrodes for 2 h in a sealed humidity chamber at 20-25 °C. Finally, TE buffer was used to remove excess target DNA.

X-Ray photoelectron spectroscopy (XPS) XPS analyses were performed using a Kratos AXIS Ultra outfitted with a monochromatic Al X-ray source (1486.7 eV). XPS was used to confirm the hybridization of target DNA, modified with Pt-NPs, to the capture probe DNA on the gold surface. Three different gold-coated slides were prepared for testing. The first was a bare gold slide cleaned with pirhana solution and rinsed with water, the second was modified with capture probe DNA and 6-mercaptohexanol, and the third was further modified by hybridization with the Pt-NP-labeled complementary target DNA. Figure 3.2 shows the spectra obtained from each of these slides in the Pt 4f region. Characteristic peaks for the Pt $4f_{7/2}$ and $4f_{5/2}$ were observed only in the case of the third slide (black curve). This result confirms hybridization and the presence of the Pt-NP labels.

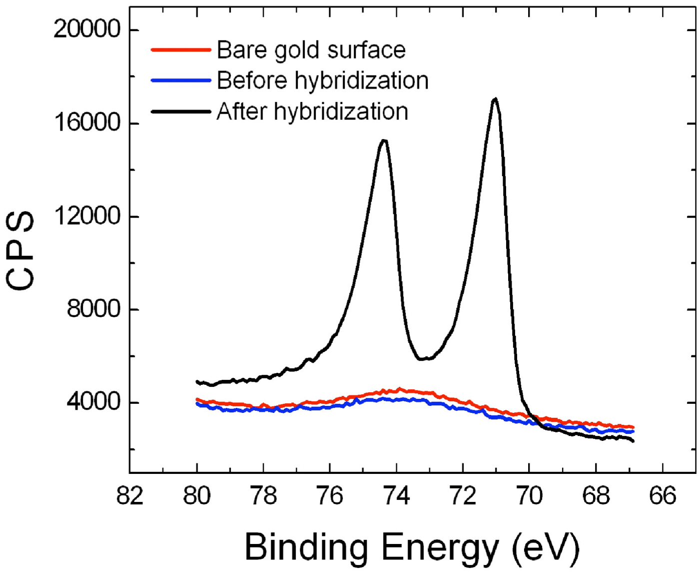

Figure 3.2. XPS spectra obtained in the Pt 4f region.

3.4 Results and Discussion

Part a of Figure 3.3 shows that the sensor consists of a microfluidic device and 3 Au electrodes. The poly(dimethylsiloxane) (PDMS) microfluidic device was prepared by a standard micromolding method.[26] The microchannel was 12 mm long, 1.75 mm wide, and 26 μm high. The 3 Au electrodes (1.00 x 0.25 mm) were microfabricated on a glass slide and configured parallel to one another at the center of the channel. Two Pt wires were placed in reservoirs at either end of the microfluidic channel and an external field was applied via a power supply.

Prior to assembly of the microfluidic device, the electrodes were modified with thiol-functionalized, 25-mer DNA capture probes by drop casting the DNA solution onto the electrodes and then back-filling vacancies within the resulting submonolayer with 6-mercaptohexanol. Next, the electrode array was exposed to a 0.1 μM solution of target DNA labeled with 4 nm Pt-NPs. Following this step and extensive rinsing, X-ray photoelectron spectroscopy confirmed the presence of Pt-NPs on the electrode surface (Figure 3.2). Finally, the PDMS block containing the microchannel was mechanically attached to the glass slide, and the channel was filled with a solution consisting of

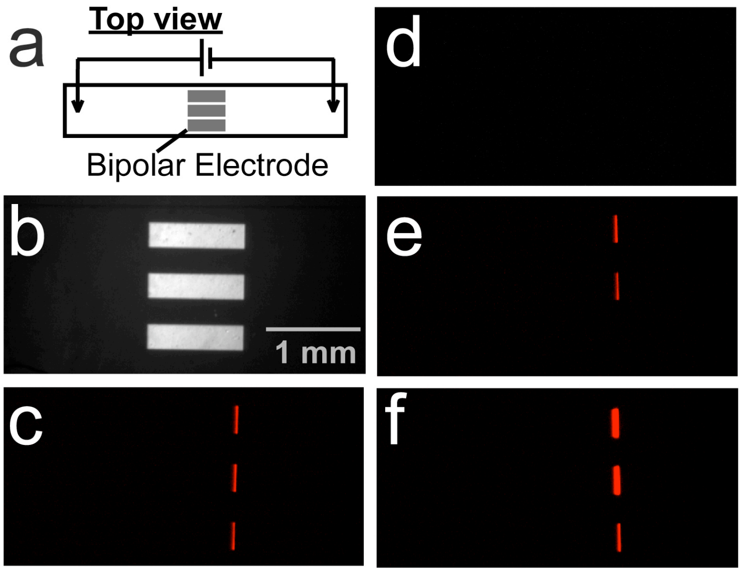

Figure 3.3. (a) Top-view schematic illustration of the microdevice. (b) Optical micrograph of the bipolar electrode configuration used to obtain the data in the other panels of this figure. False-color luminescence micrographs showing: (c) the ECL emitted at E_{tot} = 16.0 V when complementary target DNA functionalized with Pt-NPs is hybridized to probe DNA present on the electrode surface; (d) no ECL emitted at 16.0 V prior to hybridization; (e) the ECL emitted at 16.0 V when only the top two electrodes of the device are exposed to the labeled target; and (f) the ECL emission at E_{tot} = 22.0 V for the device in (e).

5.0 mM $Ru(bpy)_3^{2+}$ and 25.0 mM TPrA in 0.100 M phosphate buffer (pH 6.9).

Part b of Figure 3.3 is an optical micrograph of 3 bipolar electrodes present within the assembled microfluidic channel. Part c of Figure 3.3 is a luminescence micrograph of the same region of the fluidic channel shown in part b, but after application of a voltage of E_{tot} = 16.0 V. The red emission at the anode end of the bipolar electrodes results from ECL that is correlated to Pt-NP-catalyzed oxygen reduction at the cathode end. To ensure that the observed emission is related to the presence of the Pt-NP labels, the same experiment was performed, except without exposing the electrodes to the labeled DNA complement. In this case, no ECL is observed at E_{tot} = 16.0 V (part d), but at a higher voltage (E_{tot} = 22.0 V) ECL is observed due to direct reaction at the gold surface. The important point is that the presence of labeled DNA is signaled by ECL at all three electrodes.

The observations presented thus far can best be understood in terms of cyclic voltammograms (CVs) obtained using a classical three-electrode cell and incorporating a macroscopic gold electrode modified using the same procedures used for the microcell. Part a of Figure 3.4

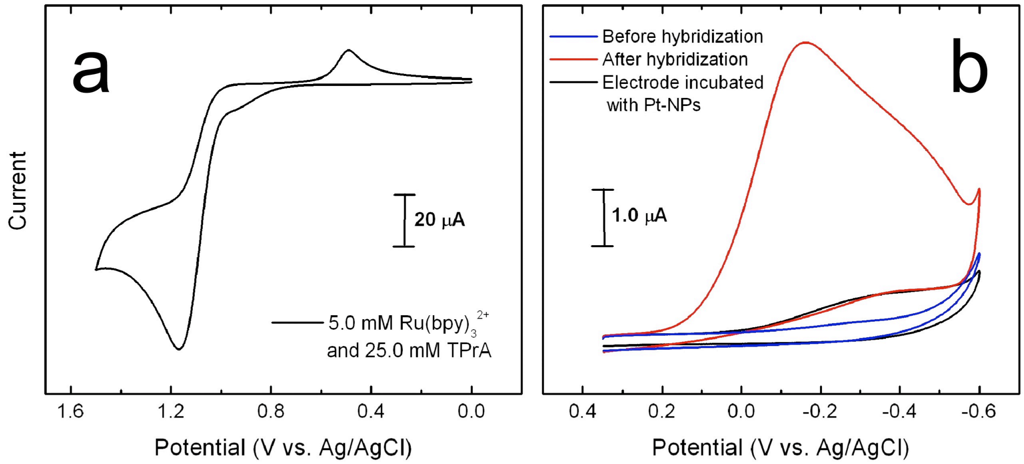

Figure 3.4. Cyclic voltammograms obtained from a macroscopic gold working electrode configured within a standard three-electrode cell. (a) The solution contained 5.0 mM Ru(bpy)$_3^{2+}$ and 25.0 mM TPrA in 0.100 M phosphate buffer. (b) The solution contained air-saturated 0.100 M phosphate buffer and the CVs were obtained after modification of the electrode with probe DNA (blue), after hybridization with Pt-NP-labeled complementary DNA (red), and after incubation of a probe-modified electrode with a 100 nM solution of free Pt-NPs (no complementary DNA, black CV). Scan rate: 100 mV/s.

shows a CV obtained in this type of cell for a solution containing both Ru(bpy)$_3^{2+}$ and TPrA present at the same concentrations used to obtain the data in Figure 3.3. Both Ru(bpy)$_3^{2+}$ and TPrA undergo oxidation at about the same potential (~1.1 V vs Ag/AgCl).[21-23] Part b of Figure 3.4 shows CVs corresponding to oxygen reduction. The red CV was obtained using a gold electrode modified with probe DNA hybridized to the complementary target labeled with Pt-NPs. A high current due to the Pt-catalyzed ORR is observed at ~ -0.1 V. Therefore, the voltage difference between the onset of Ru(bpy)$_3^{2+}$ and TPrA oxidation and oxygen reduction is ~ 1.2 V. Using the assumptions embodied in part b of Scheme 3.1 and the numerical values used to obtain the data in part c of Figure 3.3 (E_{tot} = 16.0 V, channel length = 12 mm, L_{elec} = 1.00 mm), the calculated value of ΔE_{elec} is 1.3 V. That is, the potential difference (ΔE_{elec}) required for light emission (part c of Figure 3.3) is nearly the same as the difference between the onset potentials for the ECL and ORR reactions shown in Figure 3.4. The blue CV in Figure 3.4 was obtained under the same conditions as the red CV, but in the absence of the Pt-NP-labeled DNA complement. In this case, the onset of the cathodic process is observed at a more negative potential, which is consistent with the observations discussed in relation to part d of Figure 3.3.

To demonstrate that the presence of Pt-NPs, and hence ECL emission, is directly correlated to DNA hybridization rather than to nonspecific adsorption (NSA), we prepared a macroscopic gold electrode, modified it with probe DNA, and then incubated it with a solution of Pt-NPs that were not conjugated to DNA. The resulting black CV (part b of Figure 3.4) indicates that the degree of oxygen reduction in this case is small compared to that resulting from hybridization of labeled DNA (red CV).

Parts e and f of Figure 3.3 indicate that the emission of ECL is not affected by neighboring electrodes. In this set of experiments, all three electrodes were modified with probe DNA, but only the top two were exposed to complementary DNA labeled with Pt-NPs. When E_{tot} = 16.0 V was applied across the fluidic channel, ECL was observed only at the two electrodes hybridized to the target. However, when E_{tot} was increased to 22.0 V, then the background cathodic process was initiated resulting in light emission from all three electrodes. Consistent with the model shown in part b of Scheme 3.1, emission is more intense for the upper two electrodes at this higher voltage. It is worth noting that because of the high catalytic ORR activity of the Pt-NP, a small amount of NSA from the non-target Pt-NP modified DNA could cause a false signal from the BPE.

3.5 Summary and Conclusion

The important point of this chapter is that the interfacial potential of multiple, well-defined bipolar electrodes can be controlled using just two wires. Moreover, the current flowing in all three bipolar electrodes can be indirectly observed simultaneously as light emission. Finally, chemical modification of the cathode ends of the bipolar electrodes with DNA results in a selective electrochemical array sensor. Forthcoming chapters will quantitatively address key issues such as accuracy, precision, selectivity, quantitation, and much larger numbers of bipolar electrodes.

Chapter 4: A Large-scale, Wireless Electrochemical Bipolar Electrode Microarray

4.1 Synopsis

This chapter describes a microelectrochemical array composed of 1000 individual bipolar electrodes that are controlled with just two driving electrodes and a simple power supply. The system is configured so that faradaic processes occurring at the cathode end of each electrode are correlated to light emission via electrogenerated chemiluminescence (ECL) at the anode end. This makes it possible to read out the state of each electrode simultaneously. The significant advance is that the electrode array is fabricated on a glass microscope slide and is operated in a simple electrochemical cell. This eliminates the need for microfluidic channels, provides a fabrication route to arbitrarily large electrode arrays, and will make it possible to place sensing chemistries onto each electrode using a robotic spotter.

4.2 Introduction

In this chapter we report a microelectrochemical array composed of 1000 individual bipolar electrodes (Figure

4.1a) that is controlled with just two driving electrodes and a simple power supply. The system is configured so that faradaic processes occurring at the cathode end of each electrode are correlated to light emission via electrogenerated chemiluminescence (ECL) at the anode end. This makes it possible to read out the state of each electrode simultaneously. The significant advance reported here is that the electrode array is fabricated on a glass microscope slide and is operated in a simple electrochemical cell. This eliminates the need for housing the bipolar electrode array within a microfluidic channel,[19, 27] provides a fabrication route to arbitrarily large electrode arrays, and will make it possible to place sensing chemistries onto each electrode using a robotic spotter.

Typical electrochemical experiments utilize a three-electrode configuration.[1] However, using this approach for electrode array technologies requires running a separate wire to each electrode in the array, and then measuring the current through each electrode one at a time. Because the timescale for electrochemical methods is slow compared to optical- or field-driven processes, it may be impractical to use this approach for very large arrays of electrodes.

As discussed in the previous chapter, however, we have devised a method for overcoming these limitations. Specifically, we showed that when a microfabricated wire on the order of 100-1000 μm in length is confined within a microfluidic channel, the potential difference between the electrode and the contacting solution can be controlled via a pair of driving electrodes situated at the ends of the channel.[19, 27] In contrast to a normal three-electrode configuration, where the potential of the electrode is controlled, this approach relies on controlling the potential of the solution. One obstacle with using bipolar electrodes as sensors is that there is no convenient method to directly read the current. However, we just showed that this impediment can be circumvented using ECL reporting.[19, 27]

The principles of bipolar electrochemistry have been rigorously described in several publications.[19, 27-31] Scheme 4.1a illustrates how these principles are exploited in a microarray. A voltage applied between two driving electrodes (E_{tot}) creates a linear potential gradient through the solution above the bipolar electrodes. Each bipolar electrode floats to an equilibrium potential whose value is governed by the potential gradient in solution (Scheme 4.1b). The potential difference at the electrode/solution

Scheme 4.1

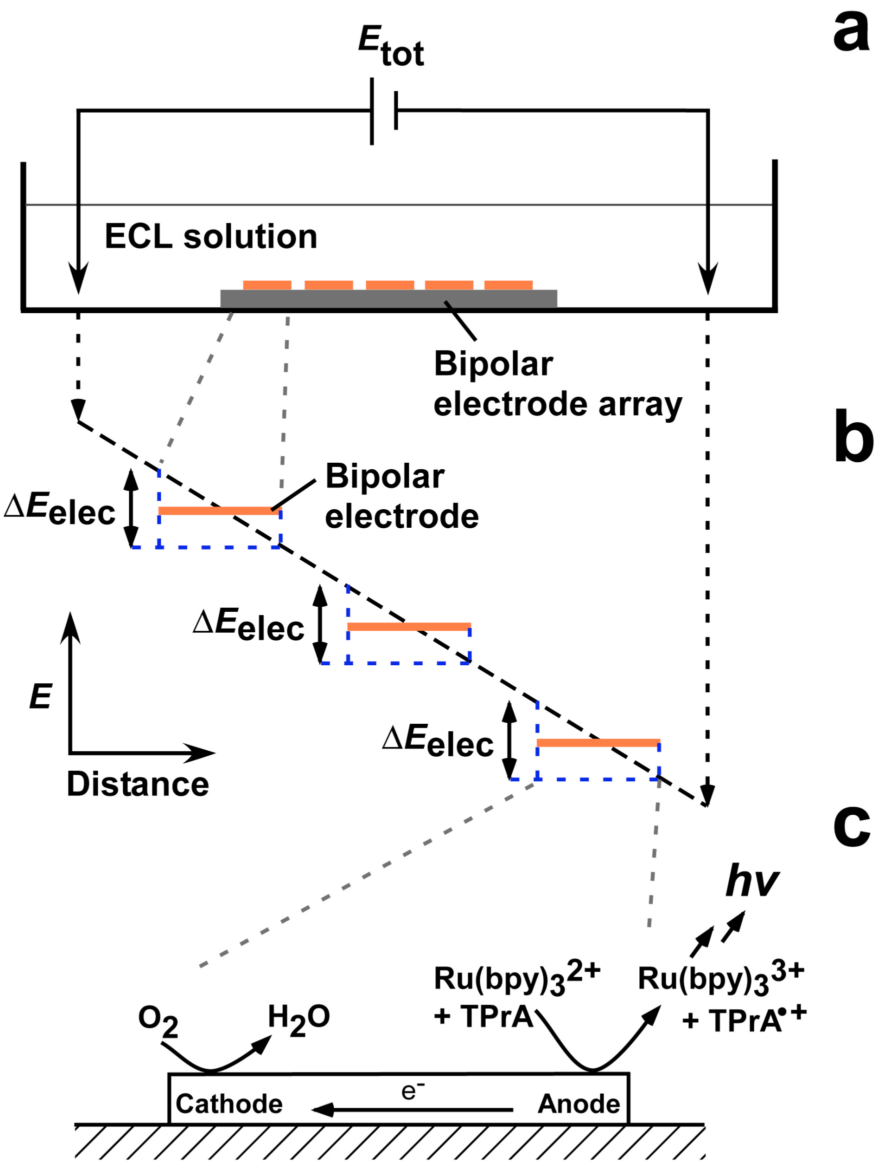
a
E_{tot}
ECL solution
Bipolar electrode array
b
ΔE_{elec}
Bipolar electrode
ΔE_{elec}
ΔE_{elec}
E
Distance
c
hv
O_2
H_2O
$Ru(bpy)_3^{2+}$ + TPrA
$Ru(bpy)_3^{3+}$ + $TPrA^{\bullet+}$
Cathode
e^-
Anode

interface will vary across the length of the electrode according to the potential gradient applied to the solution. For a linear potential gradient, the potential difference across each electrode (ΔE_{elec}) will be identical, and both anodic and cathodic overpotentials will exist on a single electrode. When the anodic and cathodic overpotentials are larger than the onset potentials for the oxidation and reduction of species in solution, then both reactions will occur simultaneously at the ends of the bipolar electrode. Due to charge neutrality, an electrochemical process at one pole of the bipolar electrode must be accompanied by an equal and opposite process at the other pole (Scheme 4.1c). In the experiments reported here, O_2 is reduced at the cathode, and $Ru(bpy)_3^{2+}$ and tri-*n*-propylamine (TPrA) are oxidized which emit ECL at the anode.[21, 22] Our group has previously quantified the ECL intensity at the anode and found that it is directly related to the rate of the cathodic reaction.[19]

In the previous chapter, we showed that bipolar electrodes can be used for sensing DNA hybridization using Pt-NPs. When Pt-NP modified DNA is present at the cathodic end of the BPE, ECL is emitted at the anodic end of the BPE. In this chapter, we will also discuss a method to specifically modify the cathodic end of each bipolar electrode in a BPE array using a robotic spotter. This allows each BPE in the array to perform different specific sensing tasks. It is necessary to add just a few simple alignment features to the BPE array design in order to accommodate the functionality of the microarrayer. These features ensure the BPEs are microfabricated at the same positions on every slide for robotic printing. Once the pin on the microarrayer is aligned with the bipolar electrodes array, the microarrayer can automatically spot different thiol-modified DNA probes at the end of each bipolar electrode.

4.3 Experimental

Chemicals and Materials Gold-coated slides used to microfabricate the BPE array were obtained from EMF (Ithaca, NY). $Ru(bpy)_3^{2+}$ and tri-*n*-propylamine were obtained from Sigma-Aldrich. Streptavidin conjugated $Ru(bpy)_3^{2+}$ was obtained from Meso Scale Discovery (Gaithersburg, Maryland).

All DNA oligonucleotides were synthesized and purified (HPLC) by Integrated DNA Technologies (Coralville, IA) and used without further purification. Three different capture probe sequences used in the robotic spotter are: CP1, (5′-S-$(CH_2)_6$-ATC CTT ATC AAT ATT-biotin-3′); CP2, (5′-S-$(CH_2)_6$-TAT ACG GTT CGC GC-3′); CP3, (5′-S-$(CH_2)_6$-CAC GAC GTT GTA AAA CGA CGG CCA G-3′).

Robotic microarrayer The robotic microarray spotter used is housed at The University of Texas Microarray Core Facility. This instrument uses a split-pin to deliver the DNA solution to the substrate surface. The 15-50 μm slit at the tip of the pin is loaded with the solution to be spotted. The pin is then moved to the desired position of the substrate and tapped onto the substrate surface to deliver the DNA solution. The volume of solution delivered can be nanoliters to picoliters depending on the tapping force between the pin and substrate.

In all the robotic spotting experiments, 10.0 μM DNA in 3x SSC buffer at pH 7.4 with 0.1% SDS and 5.0 mM tris(2-carboxyethyl)phosphine (TCEP) was used. 0.5x SSC buffer at pH 7.4 was used to clean the pin before and after each DNA spotting.

A hand-held microscope (Dino-Lite Pro AM413T, BigC, Torrance, CA) connected to a PC laptop computer was used in the spotting-pin alignment procedure.

Micrographs A microscope (Nikon AZ100, Nikon Co., Tokyo, Japan) equipped with a CCD camera (Cascade, Photometrics Ltd., Tucson, AZ) was used to obtain the optical and luminescence micrographs. Micrographs were processed using V++ Precision Digital Imaging software (Digital Optics, Auckland, New Zealand).

4.4 Results and Discussion

Wireless electrochemical bipolar electrode microarray Part a of Figure 4.1 is an optical micrograph of the microelectrode array design used in these experiments. The array consists of 1000 Au bipolar electrodes microfabricated on a glass slide. Each electrode is 500.0 μm long by 50.0 μm wide, and the electrodes are separated horizontally by 200.0 μm and vertically by 50.0 μm. The electrochemical cell was constructed of Teflon (29.0 cm x 4.0 cm) and filled with 5.0 mL of 5.0 mM $Ru(bpy)_3^{2+}$ and 25.0 mM TPrA in 0.10 M phosphate buffer (pH 6.9) (Scheme 4.1a). Two stainless steel plate electrodes were placed 18.0 mm apart with the microarray situated between them. Part b of Figure 4.1 is a luminescence micrograph of the region shown in part a after application of 85.0 V to the driving electrodes. Using geometrical arguments, an E_{tot} of 85.0 V

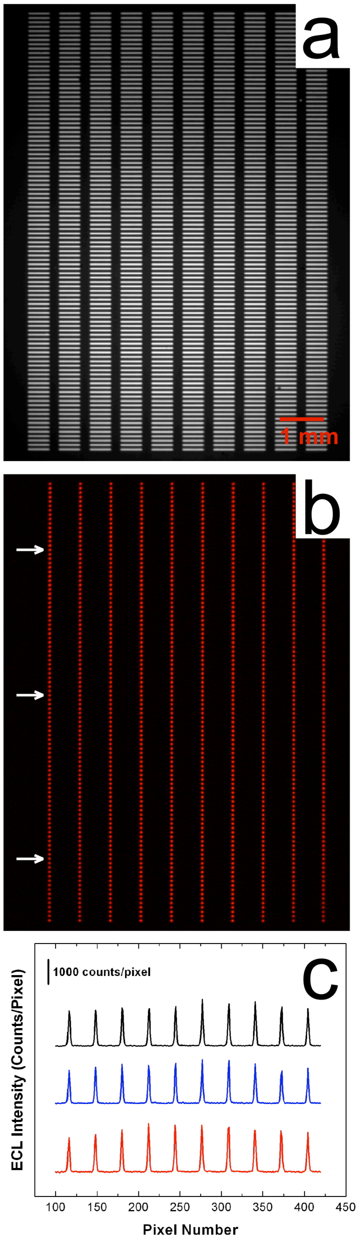

Figure 4.1. (a) Optical micrograph of the bipolar electrode array. (b) The ECL intensity emitted at E_{tot} = 85.0 V. (c) ECL intensity profile obtained from the three rows indicated by arrows.

translates to a ΔE_{elec} of ~ 2 V. This voltage is sufficient to initiate the reduction of O_2 and simultaneous oxidation of $Ru(bpy)_3^{2+}$ and TPrA at the opposite ends of the bipolar electrode. Therefore, light is emitted from the anodic end of every bipolar electrode in the array.

Part b of Figure 4.1 illustrates the uniformity of the position and area of ECL emission for each electrode. This luminescence micrograph indicates that each electrode has been subjected to an acceptably uniform electric field. Accordingly, every electrode in the array has a nearly identical anodic and cathodic overpotential. Part c of Figure 4.1 corroborates these assumptions by showing the ECL intensities from several different rows of electrodes. This plot indicates that the ECL intensity, and hence the current flowing through each electrode is nearly the same: 3877±374 counts.

Faradaic reactions on a bipolar electrode have been shown to induce a local decrease in the electric field, and the magnitude of this decrease depends on a competition between the electronic conductivity of the electrode and the ionic conductivity of the solution.[32] In our design, the solution height above the electrodes (4 mm) is large and the buffer concentration is high (0.1 M). These conditions prevent faradaic reactions on the bipolar electrodes from significantly distorting the electric field. In other words, the electrical current flowing through the bipolar electrodes is kept negligibly small compared to the ionic current flowing through the solution.

The cell design used for these experiments is not optimal, because products produced by electrochemical reactions at the driving electrodes contaminate the electrolyte solution in contact with the electrode array. This limits the operation of the array to just a few seconds before the luminescence is quenched by electrogenerated impurities. This time is sufficient for most sensor applications, however, and in any event the gold electrodes remain fully intact throughout the experiment and the array returns to its fully operational condition if the buffer solution is replaced.

The array presented here has a density of about 2,000 sensing elements/cm^2. A typical density for a fluorescence-based microarray is about 5,000 spots/cm^2,[33] and commercial electrochemical arrays[16] may have densities as large as 18,000 electrodes/cm^2. We believe it will be possible to increase the absolute number of bipolar electrodes in an array, and hence the number density, by using smaller, more closely spaced electrodes.

Immobilization of DNA using robotic spotter To fully utilize the BPE array for different specific sensing tasks, it is important to develop a method to specifically modify the cathodic end of each BPE in the array. In this experiment, a robotic spotter was used to spot different DNA sequences on a BPE array. Figure 4.2 shows the design of the BPE array for the robotic spotter. Each bipolar electrode is 800 μm long x 50 μm wide. A few alignment features on the BPE array are needed to accommodate the functionality of the microarrayer. The L-shaped alignment mark at the lower left corner of the array is used to align the gold-coated slide under a mask aligner in our photolithographic procedure. This ensures the BPEs are microfabricated at the same position on every slide.

The four circles at the corners of the BPE array are used to align the spotting-pin of the microarrayer (Figures 4.2b and Figure 4.3). This ensures the pin delivers the DNA solution at the same position at the edge of each BPE. Because of the small alignment features, a hand-held microscope connected to a laptop computer was used to assist with the alignment process. It is important that

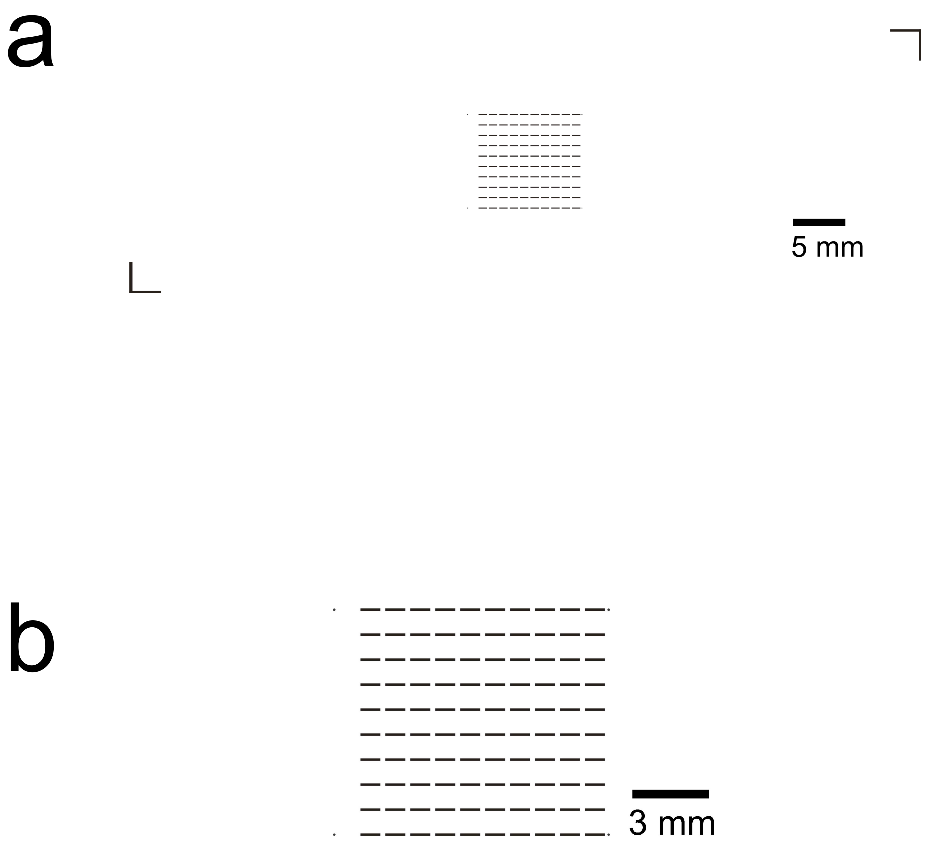

Figure 4.2. (a) Bipolar electrode array designed for the robotic microarray spotter. (b) A zoom-in image of the BPE array.

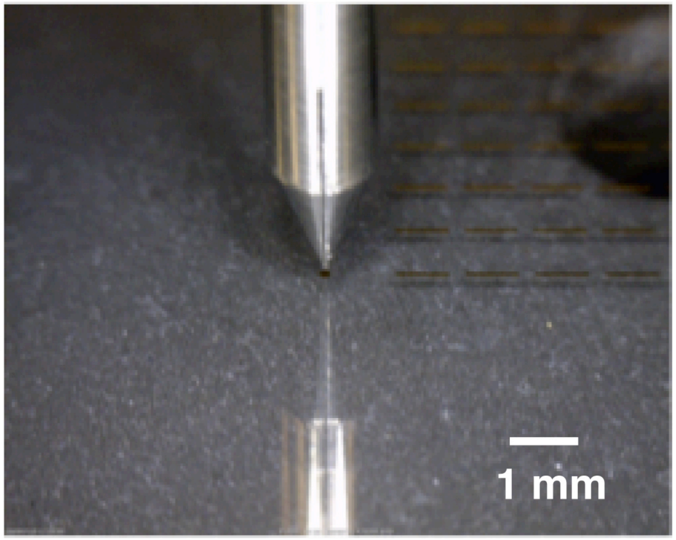

Figure 4.3. Image showing a spotting-pin aligned with a circular alignment feature on the BPE array.

the spotting-pin needs to be aligned at the centers of all four circular alignment marks. Once the BPE array and the pin are aligned (Figure 4.3), the pin will accurately deliver a drop of DNA solution to the cathodic end of each BPE.

Figure 4.4 shows a portion of an array composed of 100 BPEs spotted with three different types of DNA sequences. The dark spots shown at the end of each BPE are the dried salt of the spotted DNA solution. This experiment was carried out to demonstrate the ability of using the microarrayer to spot different DNA sequences on a large-scale BPE array. The three types of thiol-modified DNA (CP1, CP2, and CP3) solutions were first alternatively pipetted to 100 different wells of a microtiter plate for the pin to withdraw from. After that, the microarrayer was programmed to withdraw the DNA solutions from the wells and then deliver to the edge of the BPEs. The pin was continuously washed with 0.5x SSC buffer and dried three times before delivering the next DNA solution. This procedure eliminates the possibility of contaminating the DNA solutions. After the cleaning cycles, the pin would deliver another DNA solution to the next BPE from the next well. The delivering and cleaning cycles would continue

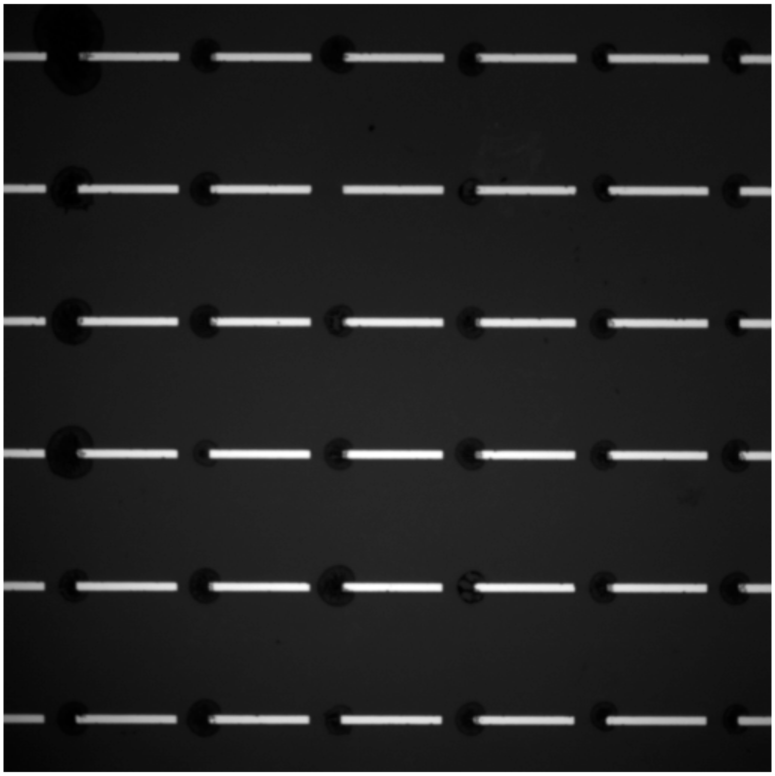

Figure 4.4. A magnified image of a 100 element bipolar electrode array spotted with different DNA solution at the edge of the bipolar electrode. Each BPE is 800 μm long.

until all 100 BPEs were spotted with the desired DNA solutions.

The importance of this experiment is that each DNA solution spotted on the BPE array was withdrawn from an individual well of the microtiter plate, although only three specific DNA sequences were used in this experiment. The new spotting method described here allows modification of each BPE in a large-scale BPE array to carry out different sensing chemistries simultaneously.

The pin of the microarrayer delivers only a very small amount of DNA onto the substrate surface and the printing process was not carried out in a humidity-controlled environment, and therefore the solution spotted on the substrate surface dries almost immediately. Therefore, it is important to demonstrate that thiol modified DNA is able to bind to the gold surface.

In this experiment, a plain gold-coated slide first spotted with CP1 DNA solution using the microarrayer and the distance between each spot is 20 μm horizontally and 20 μm vertically. CP1 DNA solution is modified with thiol at the 5′ end and with biotin at the 3′ end of the DNA oligonucleotide. After spotting, streptavidin conjugated $Ru(bpy)_3^{2+}$ was used to label the immobilized DNA on the gold surface. The immobilized DNA spots could therefore be detected by the emission of ECL from the $Ru(bpy)_3^{2+}$ label when a potential is applied at the gold-coated slide in a three-electrode spectroelectrochemical cell as shown Scheme 4.2.

After spotting, the gold-coated slide was cleaned with 0.10 M PBS for 30 s and then incubated with 1.0 μg/mL streptavidin-modified $Ru(bpy)_3^{2+}$ for 1 h. It was rinsed again with 0.10 M PBS buffer for 15 s to remove unbound $Ru(bpy)_3^{2+}$. For ECL detection of the surface-bound DNA, the slide was secured in a three-electrode spectroelectrochemical cell under a microscope (Scheme 4.2). The cell was then filled with 2.0 mL of 25.0 mM TPrA as a co-reactant with the $Ru(bpy)_3^{2+}$. For this experiment, a Pt counter electrode and an Ag/AgCl reference electrode were inserted to the cell. The emission of ECL was only observed where the DNA was spotted (Figure 4.5). This provides visual evidence that DNA immobilization occurs on the gold-coated slide surface by the robotic spotter.

Scheme 4.2

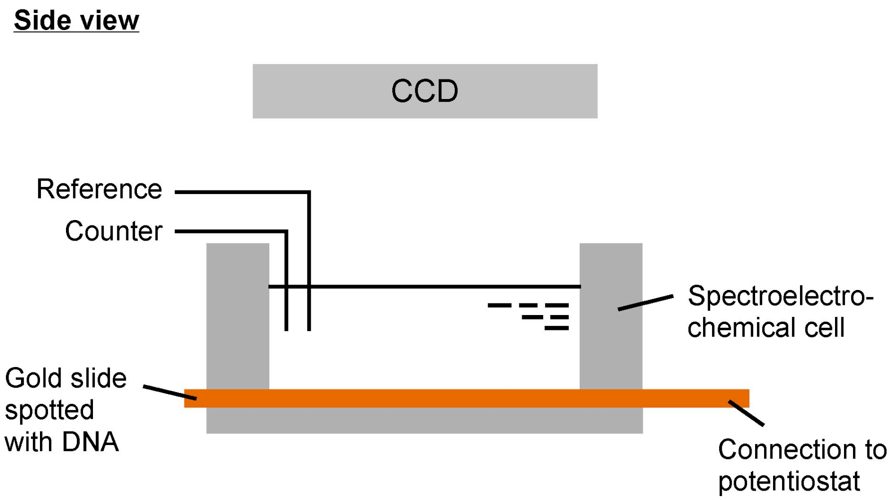
Side view
CCD
Reference
Counter
Spectroelectro-chemical cell
Gold slide spotted with DNA
Connection to potentiostat

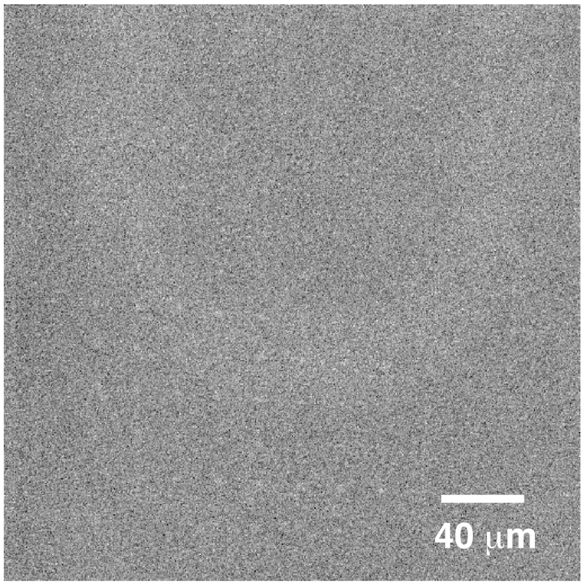

Figure 4.5. Luminescence images of the streptavidin conjugated $Ru(bpy)_3^{2+}$ labeled CP1 DNA spotted on a gold-coated slide. Exposure time: 10 s.

4.5 Summary and Conclusion

This chapter demonstrates that a microelectrochemical array composed of 1000 individual bipolar electrodes can be controlled with only two driving electrodes and a simple power supply. The emission of ECL at the anodic pole of each BPE was used to report the faradaic reaction occurs at the cathodic pole of the corresponding BPE. We also demonstrated that it is possible to specifically immobilize different capture probes DNA at the cathodic end of the BPE using a robotic spotter. This allows each BPE in the array to perform different specific sensing.

Chapter 5: A Theoretical and Experimental Framework for Understanding ECL Emission at Bipolar Electrodes

5.1 Synopsis

Bipolar electrodes are potentially useful for a variety of sensing applications, but their implementation has been hampered by an inability to easily monitor the current through such electrodes. However, current can be indirectly determined using electrogenerated chemiluminescence (ECL) as a reporting mechanism. This chapter provides a detailed theoretical analysis of ECL reporting at bipolar electrodes. In addition, experiments are described that confirm the theory. Finally, we correlate ECL intensity directly to current through the use of split bipolar electrodes. The results indicate that the lowest current that can be indirectly detected through ECL reporting is about 32 $\mu A/cm^2$, which corresponds to a reporting sensitivity of about 7200 counts/nA in the present experimental system.

5.2 Introduction

In this chapter, we show how the magnitude of the electrogenerated chemiluminescence (ECL) emission at a floating, bipolar electrode relates to the current flowing through the electrode. This correlation presents an experimental challenge, because bipolar electrodes lack external connections. We address this problem using electrode configurations that mimic the behavior of bipolar electrodes, and a rigorous, quantitative analysis of the results makes it possible to determine the emission efficiency of bipolar electrodes. This detailed level of understanding is essential for future analytical applications of bipolar electrode arrays.[19, 20, 27, 34]

We and others previously demonstrated that an isolated, conductive wire placed within a microfluidic channel can act as a bipolar electrode when a sufficiently high potential difference is applied across the solution that contacts the electrode.[3, 10, 11, 20, 27-29, 32, 35-40] Scheme 5.1 illustrates this principle. It is important to note that we assume a linear electric field because, as will be discussed later, ~99% of the total current passes through the electrolyte solution rather than through the bipolar electrode. Therefore, distortion of the electric field by faradaic current is negligible.

Our present system consists of a simple PDMS microfluidic channel that houses a microfabricated Au

Scheme 5.1

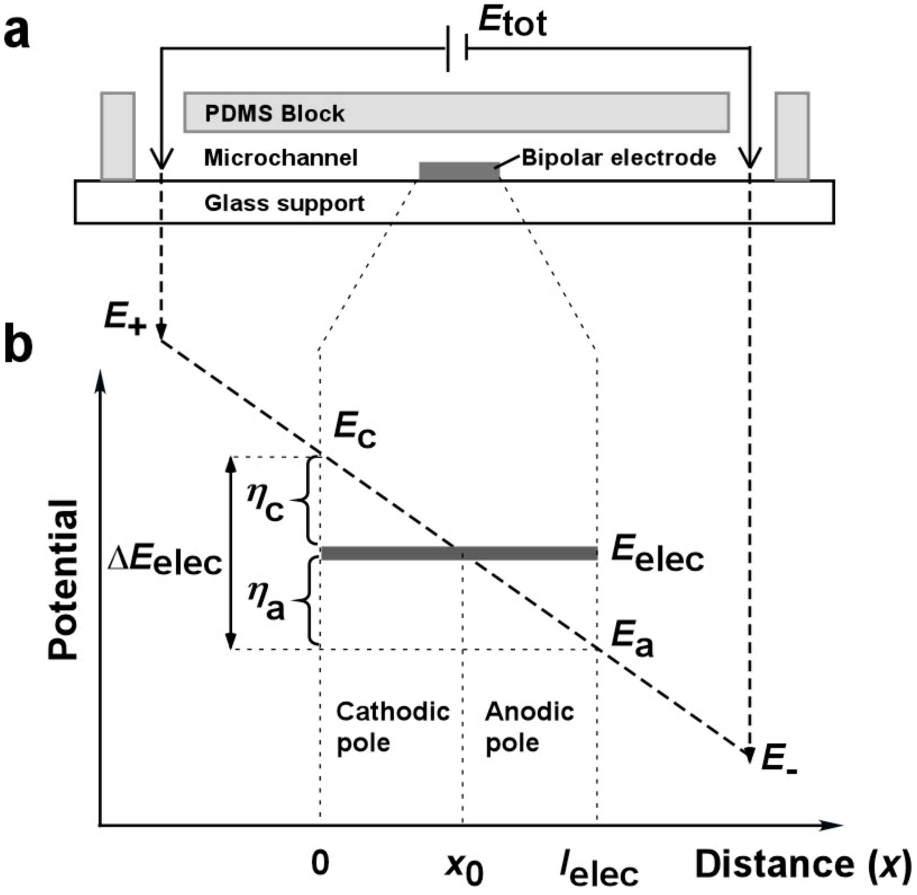
a
E_{tot}
PDMS Block
Microchannel
Bipolar electrode
Glass support
b
E_+
E_c
η_c
ΔE_{elec}
E_{elec}
η_a
E_a
Potential
Cathodic pole
Anodic pole
E_-
0
x_0
l_{elec}
Distance (x)

electrode (Scheme 5.1a). When an electric field is generated inside the channel by supplying a potential between two 'driving' electrodes at either end of the channel, faradaic reactions can occur at the Au electrode/solution interface. The reason for this behavior is that the fraction of the potential dropped in the solution along the electrode causes an interfacial potential difference that varies laterally along the electrode (Scheme 5.1b). This leads to an electrochemical reduction at the cathodic pole of the electrode and an oxidation at the anodic pole.[3] Because electroneutrality must be satisfied within the bipolar electrode, the oxidation and reduction reactions are balanced and occur simultaneously.

Our group and others have previously demonstrated that bipolar electrochemistry in a microfluidic environment can be used to build wireless sensors.[19, 20, 27, 34] Manz and co-workers[20] were the first to introduce the idea of using wireless electrochemical detection in a separation system. They used a microfluidic channel housing a floating, U-shaped Pt electrode for the detection of various amino acids in the presence of $Ru(bpy)_3^{2+}$. In their system, the amino acids acted as co-reactants for $Ru(bpy)_3^{2+}$ ECL at the anodic pole of the bipolar electrode.

Our group developed an alternative microchip ECL detection strategy at about the same time as the Manz discovery.[19, 27, 34, 41] While the Manz approach was limited to detection of co-reactants for $Ru(bpy)_3^{2+}$-based ECL (typically molecules bearing amine functionalities),[21, 23, 42] our approach could be used to detect any electrochemically active analyte. Specifically, we found that the reduction of an analyte at the cathodic pole of a bipolar electrode could be related to an ECL process at the anodic pole. The interesting aspect of this finding is that the sensing and ECL reporting events are chemically decoupled, that is, the analyte and the light emitting species do not interact chemically. As discussed in a previous chapter, we recently extended this strategy to the detection of DNA at an array of bipolar electrodes contained within a microfluidic channel.[27] In this experiment, complementary DNA labeled with Pt nanoparticles was recruited to the cathodic pole of a bipolar electrode previously functionalized with probe DNA. Once in the vicinity of the bipolar electrode, the Pt nanoparticle catalyzed the reduction of O_2. Because O_2 reduction at the cathode end of the bipolar electrode is electrically coupled to ECL emission at the anode end, light is emitted from the bipolar electrode only in the presence of the DNA target. The significant outcome of this study is its demonstration that large electrode arrays can be used to simultaneously detect the presence of biological molecules without making direct electrical contact to each electrode in the array.

Nyholm and co-workers[35, 36] recently reported on an electrochemical detection scheme using a strategy related to the one reported here. They recognized that two individual electrodes could be connected outside of a fluidic channel and thus act as a single bipolar electrode. More importantly, by connecting an ammeter between the two electrodes they were able to directly measure current. The Nyholm group has also reported a measure of the potential and current density distribution at the bipolar electrode/solution interface.[10, 30]

Duval and co-workers[28, 29, 32, 40] previously studied the fundamental principles of bipolar electrochemistry in an effort to better understand unanticipated behavior related to corrosion[28] and streaming potentials.[32] They created a rigorous mathematical model to describe the distribution of overpotential and current density along a planar bipolar electrode in an electric field. They also confirmed their model experimentally by monitoring the anodic dissolution of an Al bipolar electrode in an applied electric field.[28]

The principal objective of the present chapter is to quantitatively compare the sensitivity of light-based ECL detection with a direct measurement of the faradaic current passing through a bipolar electrode. This comparison provides a more complete understanding of the fundamental properties of bipolar electrodes, particularly as they relate to electroanalytical chemistry, a direct measure of the relative sensitivity of the two detection methods, and a theoretical framework for optimizing biosensors based on bipolar electrode arrays.

5.3 Experimental

Chemicals $Ru(bpy)_3Cl_2 \bullet 6H_2O$ (bpy = 2,2′-bipyridine) (224758) and tri-*n*-propylamine (TPrA, 239712) were purchased from Strem Chemicals and Sigma-Aldrich, respectively, and used as received unless otherwise noted in the text. Milli-Q water (Milli-Q reagent water system, Millipore, Bedford, MA) was used to prepare all aqueous solutions.

Device fabrication Standard lithographic methods were used to prepare the Au electrodes on glass slides and the poly(dimethylsiloxane) (PDMS) microfluidic channels for the microfluidic devices.[17, 26] The dimensions of the channel were: 1.2 cm long, 1.75 mm wide, and 28 μm high. A hole puncher having a diameter of 1.0 mm was used to form the reservoirs at the two ends of the microchannel. The length of the bipolar electrodes was 1.00 mm. Each half of the split bipolar electrode design was 450 *μ*m long, and they were separated by 100 *μ*m.

Luminescence micrographs A microscope (Nikon AZ100, Nikon Co., Tokyo, Japan) equipped with a mercury lamp (Nikon), and a CCD camera (Cascade, Photometrics Ltd., Tucson, AZ) were used to obtain the optical and luminescence micrographs. The luminescence micrographs were obtained under darkroom conditions with an exposure time of 1500 ms. Micrographs were processed using V++ Precision Digital Imaging software (Digital Optics, Auckland, New Zealand).

Note that the intensity of the ECL emission for a given driving potential stabilized only after the second scan (devices were scanned several times from 0 to 23 V, and only the third scan is reported). Black deposits were observed for some devices in the vicinity of location of the light emission. Control experiments have shown that the deposits correlate with the oxidation of $Ru(bpy)_3^{2+}$. The deposits can be removed from the electrode by flushing the channel with electrolyte solution.

5.4 Results and Discussion

Principles and theoretical considerations The configuration of the bipolar electrode and microfluidic system used in these experiments is shown in Scheme 5.1a. The design is similar to one used in a previous report from our group.[27] It is comprised of an Au electrode (1.00 mm x 0.25 mm) configured at the center of a microfluidic channel. The channel contains a solution consisting of 5.0 mM $Ru(bpy)_3^{2+}$ and 25.0 mM TPrA in 0.100 M phosphate buffer (pH 6.9).

When a potential, E_{tot}, is applied between two driving electrodes situated in reservoirs at either end of the microchannel, the majority of E_{tot} is dropped in the microchannel due to the high solution resistance within the channel (Scheme 5.1b). Hence, if we assume that the potential drop at the driving electrode/solution interface and within the reservoirs is negligible, then the resulting electric field (V_0) inside the channel is given by $V_0 = (E_{tot}/l_{channel})$. Here, V_0 is assumed to be constant throughout the entire length of the channel.

When a bipolar electrode is placed inside this microchannel, a fraction of E_{tot}, ΔE_{elec}, is dropped across its length, l_{elec} (eq 5.1).

$$\Delta E_{\mathrm{elec}} = E_{\mathrm{c}} - E_{\mathrm{a}} = V_0 \times l_{\mathrm{elec}} = \frac{E_{\mathrm{tot}}}{l_{\mathrm{channel}}} \times l_{\mathrm{elec}} \qquad (5.1)$$

Here, E_c represents the solution potential over the bipolar electrode at $x = 0$ and E_a is the solution potential where $x = l_{elec}$. The potential of the bipolar electrode floats, which means it is not controlled against a reference value. Accordingly, the potential of the bipolar electrode (E_{elec}) will adjust to the surrounding solution potential. Moreover, because the electrode surface experiences a continuum of solution potentials ranging from E_c to E_a, the electrode potential will adjust to an equilibrium value (E_{elec}) situated between E_c and E_a. Measured and calculated values of the bipolar electrode potential are plotted in Figure 5.1. Additional information about how this experiment was carried out, and how the data were analyzed, are discussed in the later section of this chapter.

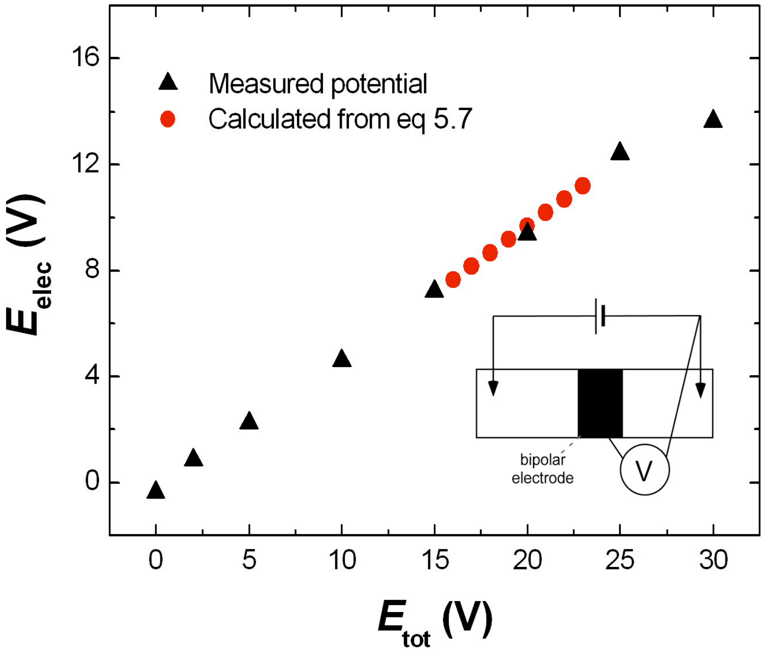

Figure 5.1. Potential of the bipolar electrode (E_{elec}) as a function of the applied driving voltage (E_{tot}). The solution contained 5.0 mM $Ru(bpy)_3^{2+}$ and 25.0 mM TPrA in 0.100 M phosphate buffer (pH 6.9). The inset shows an illustration of the experimental setup used to carry out these measurements (see text for details).

Position x_0 (Scheme 5.1b) is defined as the particular location where the potential of the solution is equal to E_{elec}. Accordingly, the electrode is divided into two poles: a cathodic pole ($x < x_0$) and an anodic pole ($x > x_0$). For both the cathodic and anodic poles, the difference in potential between the electrode and the solution at any location x is $\eta_{(x)}$, the driving force leading to an electrochemical reduction or oxidation, respectively. Because the electric field is considered constant throughout the channel, η varies linearly as a function of x across the electrode surface (eq 5.2).

$$\eta_{(x)} = E_{elec} - E_{(x)} = V_0(x_0 - x) = \frac{\Delta E_{elec}}{l_{elec}}(x_0 - x) \tag{5.2}$$

The variation of $\eta_{(x)}$ with distance across the bipolar electrode implies that the current density, $j(x)$, at the metal/solution interface is also a function of distance. The current density profile depends on both the thermodynamic and kinetic characteristics of the electrochemical processes occurring at the cathodic and anodic poles (here, the reduction of oxygen and water, and the oxidation of Ru(bpy)_3^{2+} and TPrA, respectively).

Scheme 5.2 is a representation of how the current density ($j(x)$) might vary across the surface of a bipolar

Scheme 5.2

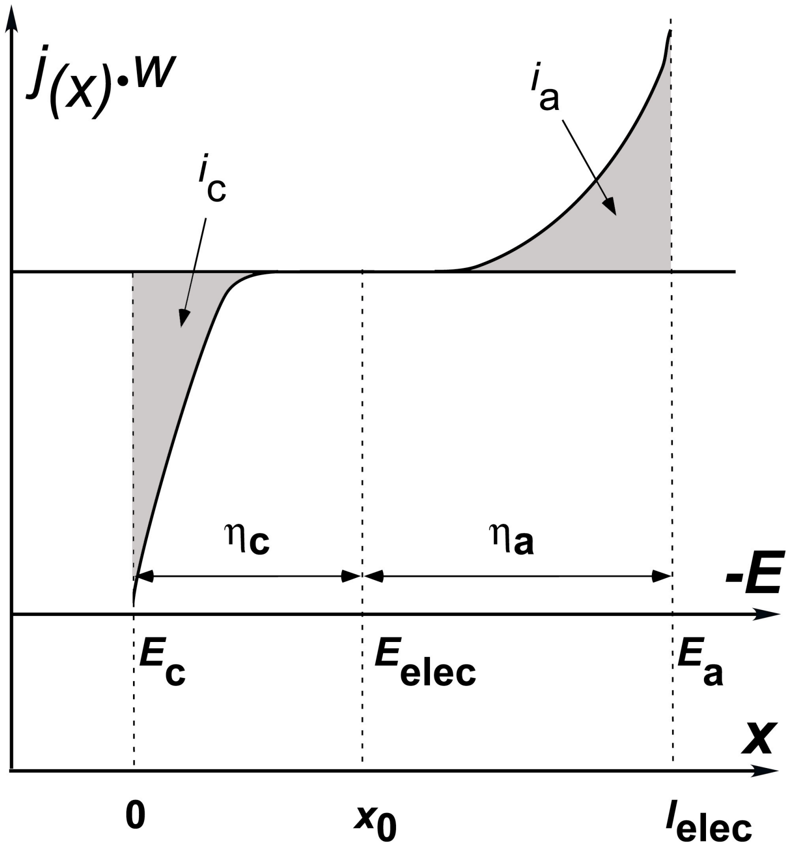

electrode. The total current density flowing through the electrode at each pole is the sum of the current densities along each pole (eqs 3 and 4 for the cathodic and anodic poles, respectively). Here, *w* is the width of the bipolar electrode.

$$i_c = w\int_0^{x_0} j(x)\cdot dx = w\int_0^{x_0} j(\eta_{(x)})\cdot dx \tag{5.3}$$

$$i_a = w\int_{x_0}^{l_{elec}} j(x)\cdot dx = w\int_{x_0}^{l_{elec}} j(\eta_{(x)})\cdot dx \tag{5.4}$$

Finally, because electroneutrality must be satisfied across the bipolar electrode, the absolute values of the anodic and cathodic currents are equal ($i = -i_c = i_a$).

Potential of the floating bipolar electrode (E_{elec}) The potential of the electrode, E_{elec}, was measured by connecting a voltmeter between the bipolar electrode and the negative driving electrode. The latter was connected to ground and acted as a reference potential for the system ($E_- = 0$ V). Control experiments confirmed that ECL emission intensity from a bipolar electrode was not affected by the presence of the voltmeter. This means that current flow through the bipolar electrode is not impeded by the presence of the voltmeter and that current leakage through the voltmeter is negligible.

Figure 5.1 provides a plot of the experimentally determined relationship between E_{elec} and E_{tot}. Clearly, the potential of the bipolar electrode varies linearly throughout the range of applied driving potential. This result is important, because it demonstrates that the potential of the bipolar electrode floats and is dependent upon the applied driving potential in a predictable way.

For the experiments reported here, the electrode is always placed at the center of the channel. Therefore, the solution potential for $x = l_{\text{elec}}/2$ is given by eq 5.5, where $E_{l_{\text{elec}}/2}$ is the solution potential halfway along the channel.

$$E_{l_{\text{elec}/2}} = \frac{E_{\text{tot}}}{2} \tag{5.5}$$

$E_{l_{\text{elec}}/2}$ can be related to E_{elec} (as long as the middle of the electrode is placed halfway along the channel) using eq 5.5. The result is given by eqs 5.6 and 5.7.

$$E_{\text{elec}} = \frac{E_{\text{tot}}}{2} + V_0(\frac{l_{\text{elec}}}{2} - x_0) \tag{5.6}$$

$$E_{\text{elec}} = E_{l_{\text{elec}}/2} + V_0(\frac{l_{\text{elec}}}{2} - x_0) \tag{5.7}$$

Eq 5.7 provides a means to calculate E_{elec} as a function of E_{tot} if x_0 is known, and this calculated relationship is compared to the experimental data in Figure 5.1. The method used to determine x_0 will be discussed later.

Solution potential difference between the ends of the electrode There is no direct method for measuring the difference in solution potential between the two ends of a bipolar electrode. However, this problem can be addressed indirectly by measuring the potential using an alternative electrode design, which is compared with a standard bipolar electrode in the inset of Figure 5.2. In essence, the middle portion of the bipolar electrode is removed in the alternative design, leaving behind two 100 μm-wide microband electrodes separated at their outer edges by 1.00 mm. This distance is the same as the length of the continuous bipolar electrode. Note that the gold microbands extend beyond the channel, which makes it possible to connect a voltmeter between them and measure the potential difference (equivalent to ΔE_{elec}) as a function of E_{tot}. The results of this experiment are provided in Figure 5.2.

It is important to note that current cannot flow through the voltmeter or the microbands in this experiment. This implies that faradic reactions cannot occur at the microbands and, therefore, do not induce depolarization, which is a local decrease of the electric field in the solution over the bipolar electrode.[32] In the case of a single, continuous bipolar electrode (the design above the

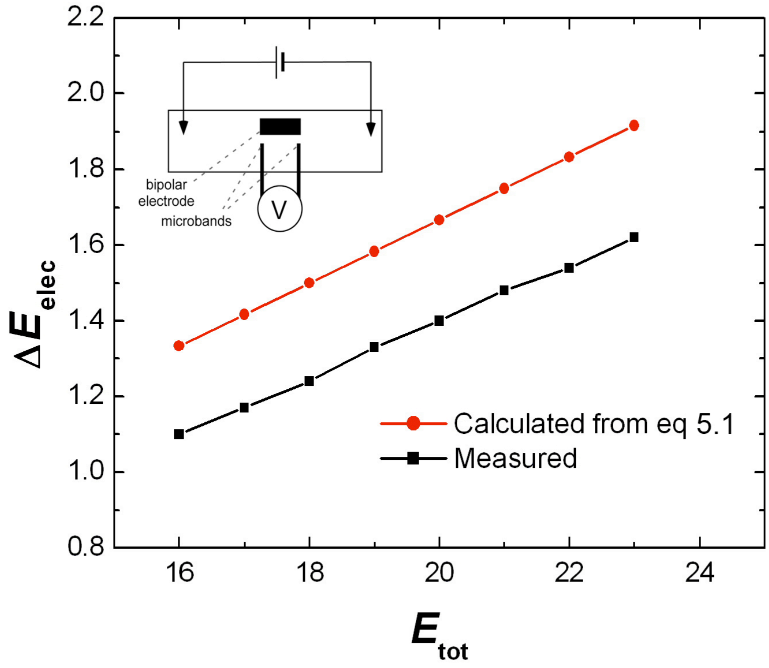

Figure 5.2. Plot of the difference in potential between two microbands (inset, ΔE_{elec}) as a function of the applied driving voltage (E_{tot}). This value corresponds to the total overpotential between the two ends of a continuous bipolar electrode. The solution contained 5.0 mM $\mathrm{Ru(bpy)_3^{2+}}$ and 25.0 mM TPrA in 0.100 M phosphate buffer (pH 6.9). The inset shows an illustration of the experimental setup used to carry out these measurements (see text for details).

microbands in the Figure 5.2 inset), depolarization occurs when the ionic current through the solution is low compared to the faradaic current passing through the bipolar electrode. In other words, the extent of depolarization will depend on the fraction of the total current that is carried by the bipolar electrode. The important point is that the continuous bipolar electrode and microbands represented in the inset of Figure 5.2 are analogous, because even in the case of a single, continuous bipolar electrode, there is little depolarization. This is because the buffer concentration is always kept high. Experiments discussed later show that under these conditions, ~99% of the current passes through the solution and just ~1% through the electrode.

The experimental results shown in Figure 5.2 can be compared to a calculated value by combining the geometrical arguments expressed in eq 5.1. This equation is plotted as the red line in Figure 5.2. The results indicate that the measured value of ΔE_{elec} is lower than the calculated value. We conclude that the true potential drop across the channel is less than the drop between the two driving electrodes. That is, a portion of the applied potential, E_{tot}, is lost at the driving electrode/solution interface or within the reservoirs at either end of the channel. The potential difference between the two lines in Figure 5.2 suggests that ~3 V of E_{tot} are dropped outside the microfluidic channel. Qualitative confirmation of this speculation comes from the observation of ECL emission from the positive driving electrode. An ideal experimental configuration would employ infinitely narrow microbands for the measurement of ΔE_{elec}, because some potential will be dropped across the microbands. This will result in an underestimation of ΔE_{elec}. We have chosen to use microbands having a width of just 100 μm to minimize this error.

Estimation of the current flowing through the bipolar electrode In his seminal paper,[28] Duval and coworkers predicted the current flow in a bipolar electrode. Their elucidation of the Butler-Volmer equations for the anodic and cathodic processes led directly to the determination of x_0 as a function of the applied electric field. The determination of x_0 is then sufficient to establish a complete linear relationship between distance and overpotential (eq 5.2). Therefore, when eq 5.2 is combined with the Butler-Volmer equation, it is possible to establish the current density profile $j(x)$. Finally, direct mathematical integration of an expression for $j(x)$

over the area of each pole leads to the value of the current (Scheme 5.2). However, Duval's prediction is only valid when the electron-transfer kinetics of the faradaic reactions occurring on the bipolar electrode are explicitly known. In our system this is not the case, and the complexity of the redox processes (oxygen and water reduction at the cathode and $Ru(bpy)_3^{2+}$ and TPrA oxidation at the anode) hinders our ability to define the reaction kinetics. Therefore, we are forced to determine $j(x)$ semi-empirically.

The first step necessary for determining $j(x)$ was to empirically measure the current density vs. stepped potentials ($j(E_{step})$) for an electrode contained within an air-saturated $Ru(bpy)_3^{2+}$/TPrA solution. This experiment was executed by configuring a traditional three-electrode cell within a microfluidic device, and then carrying out a series of chronoamperometric experiments. Specifically, the fluidic system was filled with solution, the potential of an Au microband electrode situated near one of the reservoirs was stepped to different potentials, E_{step} (versus a reference electrode), and the resulting current transient was measured. Further details about this experiment are provided in the later section (Scheme 5.3). The data, which is a plot of j as a function of E_{step}, are provided in Figure 5.3.

We now focus on extracting $j(x)$ from $j(E_{\mathrm{step}})$. This transition requires several steps. First, we converted $j(E_{\mathrm{step}})$ to a secondary plot of current density vs. overpotential, $j(\eta_{(x)})$ (top axis of Figure 5.3). This is accomplished by defining an equilibrium potential, E_{zcd} (zcd = zero current density), in the $j(E_{\mathrm{step}})$ plot. E_{zcd} is comparable to E_{elec} derived from the plot of $j(\eta_{(x)})$. This equivalence between E_{zcd} and E_{elec} establishes a reference point for converting $j(E_{\mathrm{step}})$ to $j(\eta_{(x)})$ (Figure 5.3). A rigorous mathematical explanation of this conversion is provided in a later section.

The conversion of $j(\eta_{(x)})$ to $j(x)$ requires a simple conversion of the η-axis to values of x using the linear relationship in eq 5.2. Unfortunately, eq 5.2 contains an unknown value, x_0, which must be derived mathematically before $j(\eta_{(x)})$ can be converted to $j(x)$. We describe the mathematical derivation of x_0 in a later section, but calculated values of x_0 for several driving voltages are listed in Table 1. With x_0 in hand, it is possible to determine $j(x)$ and then determine the amount of current flowing through the bipolar electrode as a function of E_{tot}.

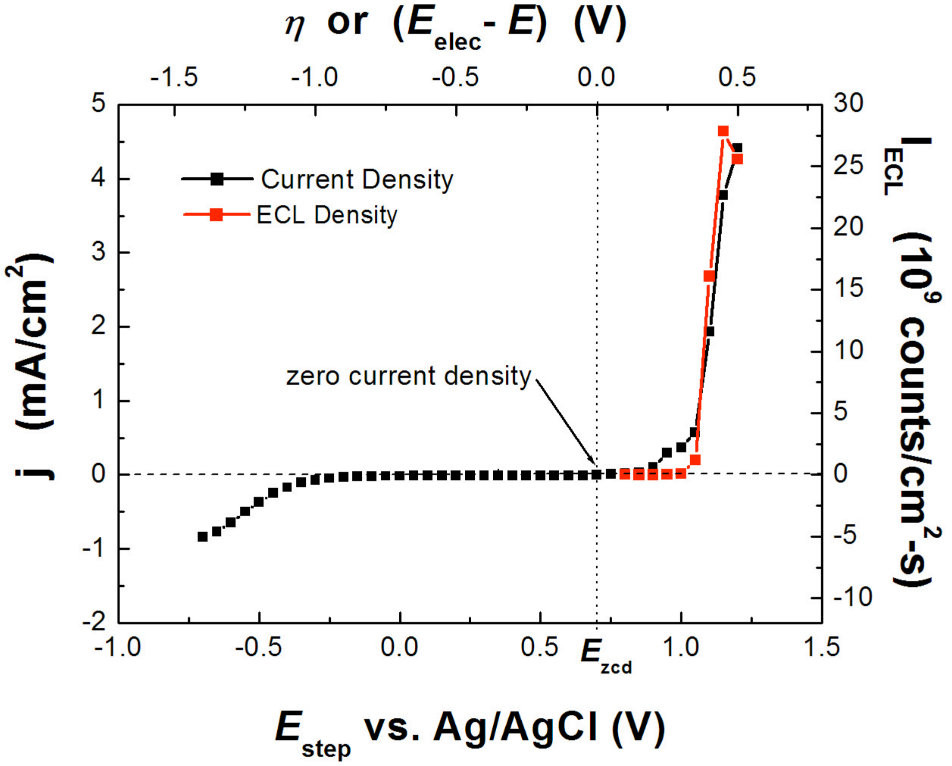

Figure 5.3. Current density (j) and ECL emission density (I_{ECL}) measured at a microband electrode. The solution contained 5.0 mM $Ru(bpy)_3^{2+}$ and 25.0 mM TPrA in 0.100 M phosphate buffer (pH 6.9). These measurements were obtained using a standard three-electrode cell (Scheme 5.3). Bottom axis: potential of the working electrode vs. Ag/AgCl. Top axis: overpotential measured from the zero current density (ZCD) point.

The current density will be the same along the width of the electrode. Therefore, the linear current density, which is simply $j(\mathrm{x})\bullet w$ (w is the width of the bipolar electrode), represents the total current density at a given position x along the length of the electrode. A series of linear current density plots, $j(\mathrm{x})\bullet w$ vs. x, for different values of E_{tot}, are provided in Figure 5.4. Finally, graphical integration of the linear current density curves yields a predicted current value through the bipolar electrode for a specific applied driving voltage. Several calculated current values are listed in Table 1.

Potentiostep experiment using a three-electrode configuration This experiment was designed to obtain current density and ECL emission intensity density from a solution containing 5.0 mM $\mathrm{Ru(bpy)_3^{2+}}$ and 25.0 mM TPrA in 0.100 M phosphate buffer (pH 6.9) using the same configuration used to collect data from the continuous and split bipolar electrodes (Figure 5.6). As shown in Scheme 5.3, the working electrode is a microband in the channel that is very close to the well. The reference electrode (Ag/AgCl) is placed in the well as close as possible to the microband. IR drop is considered to be negligible under these conditions. Experimental evidence for this assumption

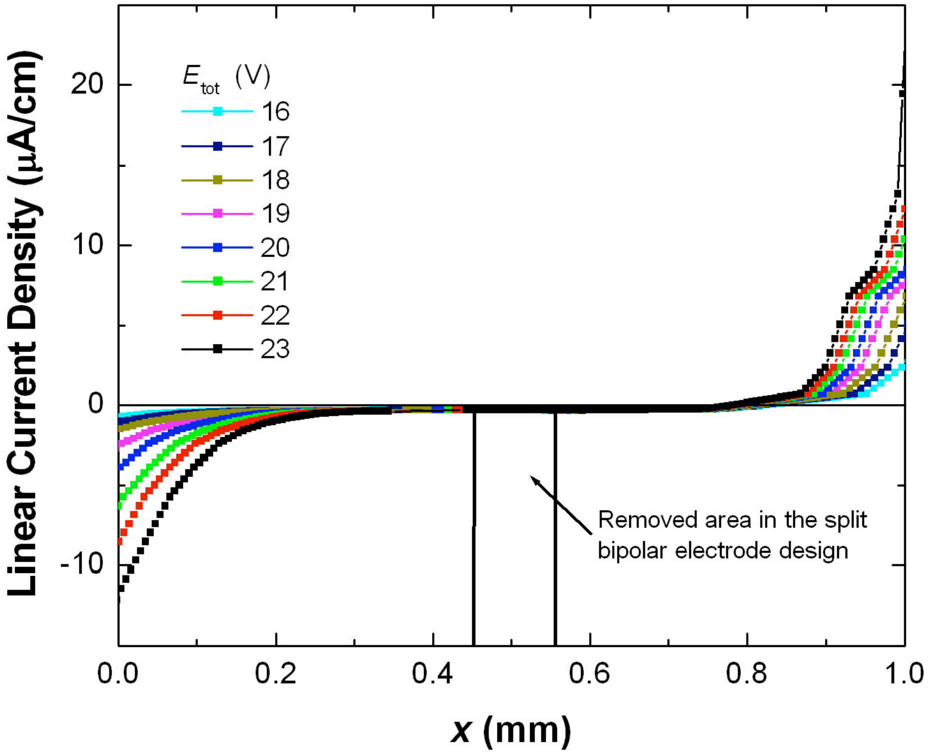

Figure 5.4. Linear current density as a function of position along a bipolar electrode for different values of the applied driving voltage (E_{tot}). The solution contained 5.0 mM $Ru(bpy)_3^{2+}$ and 25.0 mM TPrA in 0.100 M phosphate buffer (pH 6.9).

Scheme 5.3

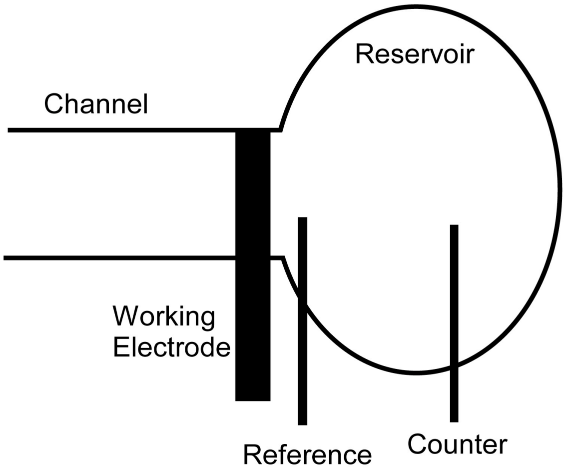

comes from the observation that at sufficiently positive potentials, the ECL intensity was evenly distributed across the surface of the electrode. The current density, $j(E_{\text{step}})$, is the current collected at the working electrode 5 s after the step divided by the surface area of the microband. The linear current density is then obtained by multiplying $j(E_{\text{step}})$ by the width of the microfabricated bipolar electrode, because by symmetry the current density will be uniform in this axis (defined as the y axis). In the direction parallel to the long axis of the channel (defined as the x direction) there is an overpotential gradient along the electrode. The bipolar electrode can thus be divided conceptually into a series of individual microbands (x-dx, x, x+dx …) having lengths dx that simultaneously undergo a potential step at different overpotentials ($\eta(x\text{-d}x)$, $\eta(x)$, $\eta(x\text{+d}x)$…), as shown in Scheme 5.4. Consequently, chronoamperometric measurements for the different overpotentials ($\eta(x\text{-d}x)$, $\eta(x)$, $\eta(x\text{+d}x)$…) using a three-electrode cell are equivalent to the measurement of the current density that would be observed at each particular virtual microband.

Scheme 5.4

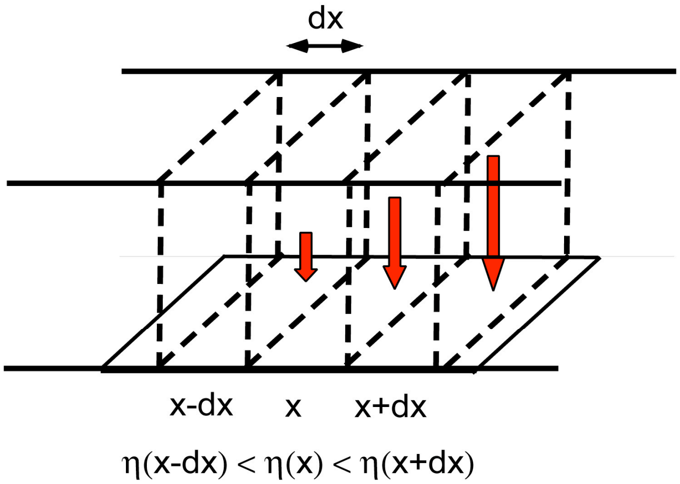

Conversion of $j(E_{\mathrm{step}})$ to $j(\eta_{(x)})$ The conversion of $j(E_{\mathrm{step}})$ to $j(\eta_{(x)})$ presents a problem. E_{step} was measured vs. Ag/AgCl, whereas the overpotential in a bipolar system is referenced against an equilibrium potential, E_{elec}. Fortunately, $j(E_{\mathrm{step}})$ contains an inflection point, E_{zcd} (zcd = zero current density), and it is comparable to E_{elec} because both E_{elec} and E_{zcd} are points of zero net current density. Therefore, both terms may be treated as equilibrium potentials. Treating E_{zcd} as an equilibrium potential means that any potential difference from equilibrium, E_{step}-E_{zcd}, can be treated as an overpotential, η. We can, therefore, use $\eta = E_{\mathrm{step}}-E_{\mathrm{zcd}}$ to convert $j(E_{\mathrm{step}})$ to $j(\eta_{(x)})$.

Determination of x_0 To convert $j(\eta_{(x)})$ to $j(x)$, every term in eq 5.2 must have a known value. Unfortunately, the x_0 term must be determined mathematically. To find x_0 we first define the boundaries of the bipolar electrode as $x = 0$ and $x = l_{\mathrm{elec}}$. Using eq 5.2, we can express the overpotential at each boundary as η_{c} for $x = 0$ and η_{a} for $x = l_{\mathrm{elec}}$.

$$\eta_{\mathrm{c}} = -(\Delta E_{\mathrm{elec}} / l_{\mathrm{elec}})\, x_0 \tag{5.8}$$

$$\eta_{\mathrm{a}} = \Delta E_{\mathrm{elec}} - (\Delta E_{\mathrm{elec}} / l_{\mathrm{elec}})\, x_0 = \Delta E_{\mathrm{elec}} + \eta_c \tag{5.9}$$

Now if we can calculate the values of η_c and η_a we will know the value of x_0. To find η_c and η_a we must invoke the assumption of electroneutrality.

$$P_a(\eta_a) = -P_c(\eta_c) \tag{5.10}$$

Eq 5.10 states that, due to electroneutrality, the current (or power) delivered to each pole of the bipolar electrode must be equal. Graphically, this means that the area under the curve in the plot of j vs. η should be equal on either side of the equilibrium point, E_{elec}. Integrating $j(\eta_{(x)})$ over each pole yields eqs 5.11 and 5.12.

$$P_a = \int_0^{\eta} j'(\eta) \cdot d\eta \quad \text{for } \eta > 0 \tag{5.11}$$

$$P_c = \int_{\eta}^{0} j'(\eta) \cdot d\eta \quad \text{for } \eta < 0 \tag{5.12}$$

These integrals can be solved graphically in two steps to give functions for P_a and P_c. First, the plot of j vs. η (Figure 5.3) is graphically integrated for a series of arbitrary values of η. Second, the resulting values are plotted and fitted using exponential functions (Figure 5.5).

Figure 5.5 shows the integral curve of $j(\eta)$. The latter was graphically integrated taking η and 0 as the integration limits. The two fitting curves, representing

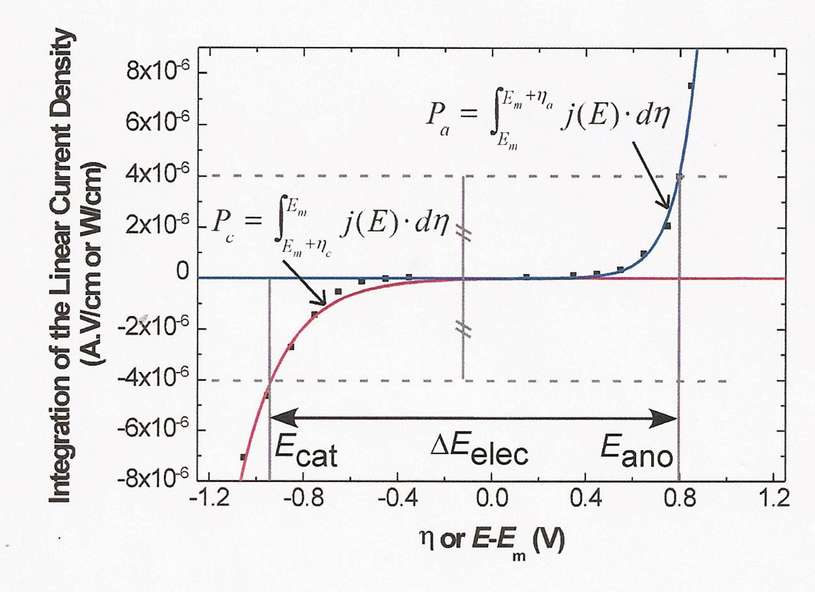

Figure 5.5. Plot of integration of the linear current density vs. overpotential (η). This plot is used to determine P_a and P_c graphically.

the functions P_a and P_c, were fitted using Origin software. The resulting exponential functions are defined in eqs 5.13 and 5.14.

$$P_\mathrm{a} = P_\mathrm{a}^0 \exp(\alpha_\mathrm{a}\eta) \tag{5.13}$$

$$P_\mathrm{c} = -P_\mathrm{c}^0 \exp(-\alpha_\mathrm{c}\eta) \tag{5.14}$$

with $P_\mathrm{a}, P_\mathrm{c}, \alpha_\mathrm{a}, \alpha_\mathrm{c} > 0$.

Eqs 5.9 and 5.10 can now be solved simultaneously for η_c and η_a using these exponential functions of P_a and P_c. The resulting solutions for η_c and η_a are given in eqs 5.15 and 5.16.

$$\eta_\mathrm{c} = \frac{1}{\alpha_\mathrm{a} + \alpha_c}\left[\ln\left(\frac{P_\mathrm{c}^0}{P_\mathrm{a}^0}\right) - \alpha_\mathrm{a}\Delta E_\mathrm{elec}\right] \tag{5.15}$$

$$\eta_\mathrm{a} = \Delta E_\mathrm{elec} + \eta_\mathrm{c} \tag{5.16}$$

Every term in eq 5.15 has a known value, therefore, the values of η_c and η_a can be calculated. Several values of η_c and η_a for different driving voltages are provided in Table 1. Rearranging eq 5.8 then gives a straightforward expression (eq 5.17) for determining the values of x_0 using η_c.

$$x_0 = -\frac{l_\mathrm{elec}}{\Delta E_\mathrm{elec}}\eta_\mathrm{c} \tag{5.17}$$

Several calculated values of x_0 for different driving voltages are also listed in Table 5.1.

Direct measurement of the current at a split bipolar electrode To directly compare the currents calculated in Table 1 to experimental measurements, the two halves of a split bipolar electrode design are connected by an ammeter (Figure 5.6a). This provides a direct measure of the electric current induced in the bipolar electrode by the two driving electrodes. The results in Figure 5.4 show that there is little or no faradaic electron transfer in the center of a bipolar electrode, and this suggests that the electrochemical properties of the split electrode should be the same as a continuous bipolar electrode. However, to experimentally confirm the congruency of the split and continuous bipolar electrodes, one of each design was placed side-by-side in the same channel during every experiment (Figure 5.6b), and the ECL emission from each was measured. As shown in parts a and b of Figure 5.6, the outermost edge-to-edge length (l_{elec}) of both types of electrodes was the same. Note that the connections to the split electrode are placed at the inner edge of each half electrode to ensure that faradaic reactions only occur at the ends of the electrode (and not on the contacts).

Table 5.1. Calculated values of key parameters as a function of the applied driving voltage. Only ΔE_{elec} was measured. η_c and η_a are determined by resolution of eqs 15 and 16, x_0 is from eq 17, i is determined from graphical integration of the linear current density, E_{elec} (eq 7), and the ECL intensity is determined from graphical integration of the linear ECL density.

E_{tot} (V)	DE_{elec} (V)	η_c (V)	η_a (V)	x_o	i_a (nA)	E_{elec} (V)	ECL intensity (counts)
16.0	1.10	-0.90	0.20	0.82	20	7.7	-
17.0	1.17	-0.95	0.22	0.81	27	8.2	-
18.0	1.24	-0.99	0.25	0.80	34	8.7	-
19.0	1.33	-1.06	0.27	0.79	44	9.2	6617
20.0	1.40	-1.10	0.30	0.79	54	9.7	13763
21.0	1.48	-1.16	0.32	0.78	70	10.2	48024
22.0	1.54	-1.20	0.34	0.78	89	10.7	136457
23.0	1.62	-1.26	0.36	0.78	117	11.2	374859

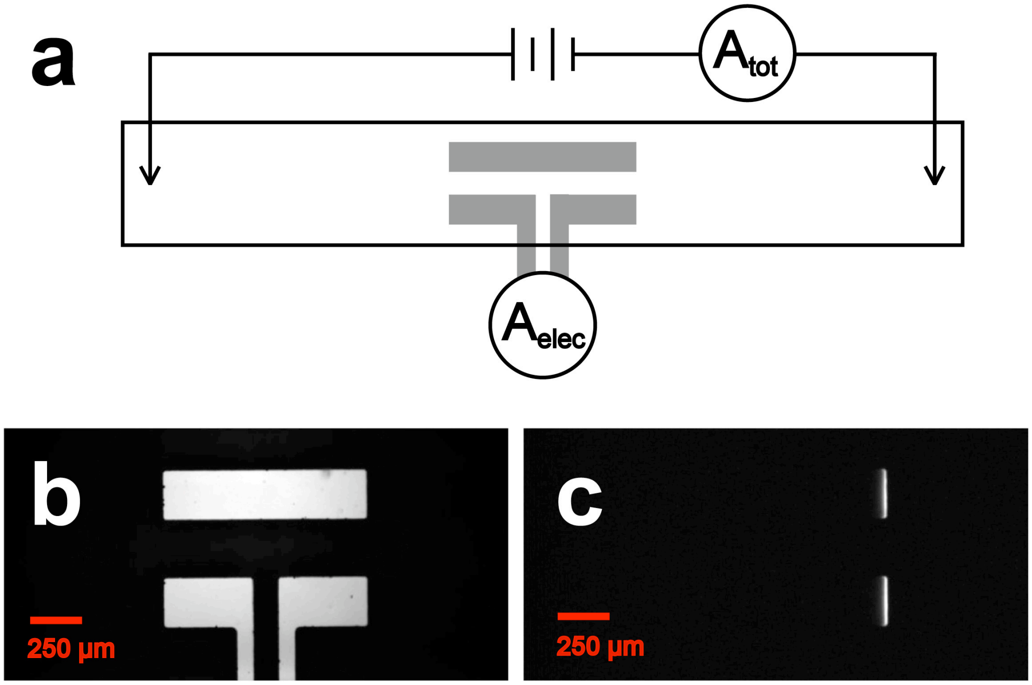

Figure 5.6. (a) A schematic representation of the experimental configuration used to quantify the extent of depolarization. (b) Optical micrograph of the electrode configuration corresponding to (a). (c) Luminescence micrograph for E_{tot} = 22 V. The ECL intensities from the continuous and split bipolar electrodes were 0.19 and 0.22 x 10^6 counts, respectively. The solution contained 5.0 mM $Ru(bpy)_3^{2+}$ and 25.0 mM TPrA in 0.100 M phosphate buffer (pH 6.9).

The ECL emission from luminescence micrographs like the one shown in Figure 5.6c have been quantified using digital imaging software, and we find that intensities from the two electrode designs are always within 10% of one-another. Moreover, when the direct connection (via a copper wire) between the two halves of the split electrodes is replaced by an ammeter (Figure 5.6a), the correspondence of the ECL emission is maintained. A second ammeter may be connected between a driving electrode and the power supply to measure the total current through the system (Figure 5.6a). For E_{tot} = 20 V, the total current is ~65 μA compared to 54 nA measured through the split bipolar electrode. The ratio of these two measured values indicates that the electric field will decrease less than 0.1% over the bipolar electrode and that the effects of depolarization are negligible. These results prove that the split design is equivalent to a continuous bipolar electrode, and that the split design can be used to directly measure the current passing through a bipolar electrode.[36]

In Figure 5.7, a plot of the current measured through a split bipolar electrode vs. the voltage applied across the channel (E_{tot}) is compared to the current calculated using Figure 5.4. The close agreement between calculated

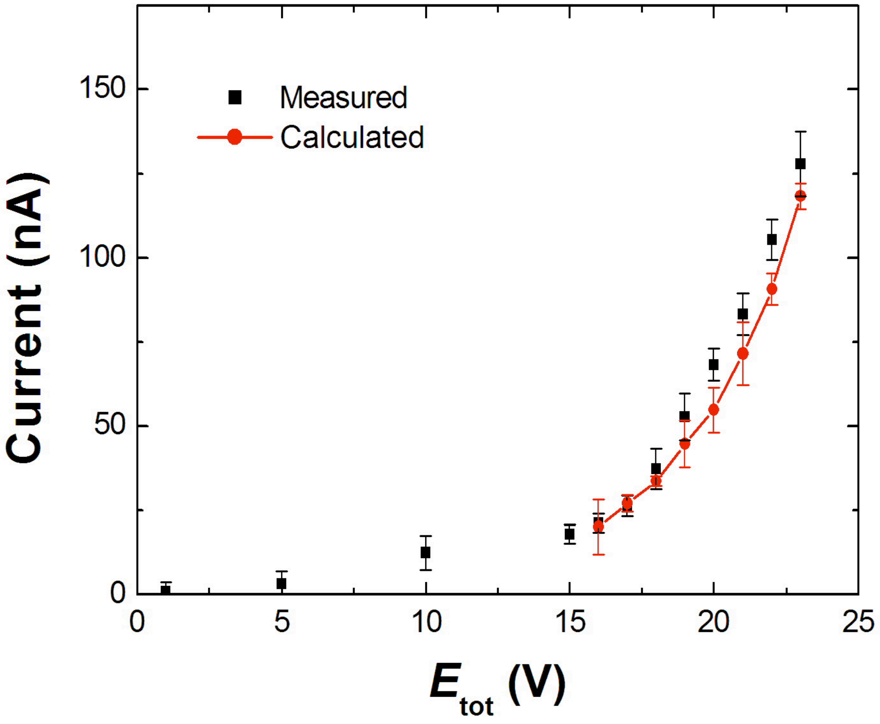

Figure 5.7. Plot of the current for a split bipolar electrode vs. the applied driving potential (E_{tot}). The calculated values (Table 5.1 and red curve) are averages from the integration of the current density over both cathodic and anodic poles, respectively. The error bars represent the standard deviation. The solution contained 5.0 mM $Ru(bpy)_3^{2+}$ and 25.0 mM TPrA in 0.100 M phosphate buffer (pH 6.9).

and measured values suggests that the assumptions used for the calculations are valid. Recall that a particularly important postulate was that the potential drop over the length of the electrode is linear, and thus the effect of depolarization negligible, under the conditions used for these experiments.

Determination of the ECL intensity profile and the total ECL intensity Just as the current density profile (Figure 5.4) can be semi-empirically determined, the ECL density profile $I_{\mathrm{ECL}}(x)$ can also be estimated using $\eta(x)$. This is done as follows. First, ECL density is measured as a function of step potential, $I_{\mathrm{ECL}}(E_{\mathrm{step}})$, using the same method (Scheme 5.3) used to generate the results in Figure 5.3. Second, using the approach described earlier for the current density, the empirically determined ECL density, $I_{\mathrm{ECL}}(E_{\mathrm{step}})$, was used to generate a plot corresponding to $I_{\mathrm{ECL}}(\eta)$. The results of these first two steps are displayed as the red line in Figure 5.3. Third, the values of $I_{\mathrm{ECL}}(\eta)$ and $\eta(x)$ were used to determine $I_{\mathrm{ECL}}(x)$ for different values of E_{tot}.

In contrast to the current density profile, the ECL profile can easily be measured directly. Figure 5.8 represents both measured and calculated ECL intensity

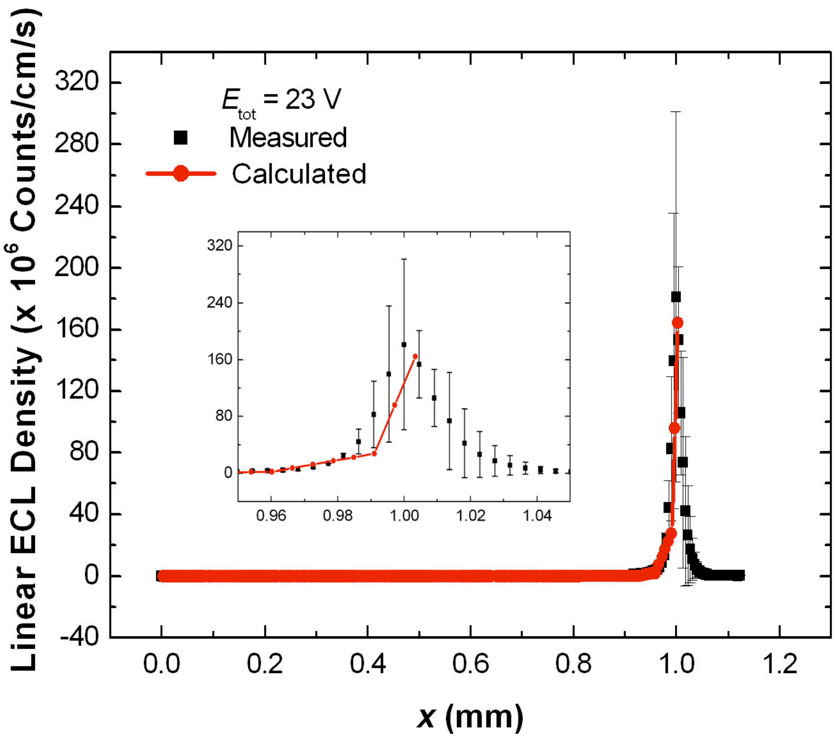

Figure 5.8. Plot of the linear ECL emission density for a bipolar electrode as a function of position along the electrode. The inset shows an expanded view of the peak. The solution contained 5.0 mM $Ru(bpy)_3^{2+}$ and 25.0 mM TPrA in 0.100 M phosphate buffer (pH 6.9).

profiles for E_{tot} = 23.0 V. The correspondence between the measured and calculated values of the ECL is striking, and both indicate that (at this driving potential) the overpotential required to drive the ECL reactions is only found at the end of the bipolar electrode.

Integration of the ECL density profile (Figure 5.8) leads to the total intensity of light observed at the bipolar electrode. Figure 5.9 compares the measured intensities for the two electrode designs with the integration of calculated ECL density profiles as a function of E_{tot}. The calculated intensities are, on average, a little lower than the measured values, but nevertheless the correspondence between the measured and calculated intensities is quite satisfactory.

Relationship between the faradaic current and the ECL intensity Figure 5.10 shows the relationship between the total ECL intensity and the faradaic current. A key point is that, for our measurement system, a threshold current of ~75 nA must be attained before ECL is detected. Thereafter, the ECL intensity increases linearly as a function of the faradaic current. This linear relationship indicates that ECL emission can be easily correlated to the faradaic current, and that therefore ECL emission will

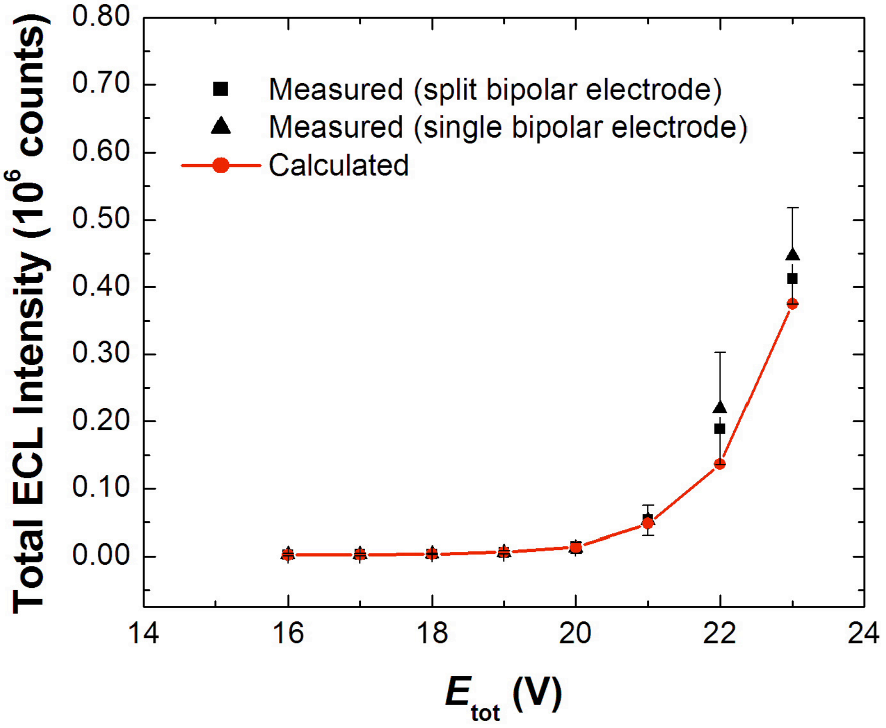

Figure 5.9. Simultaneous measurement of the total ECL intensity for both split and continuous (single) bipolar electrodes as a function of the driving potential (E_{tot}). The measured values represent the average of four independently prepared devices. The red line represents the total ECL intensity estimated from the integration of the calculated ECL profiles.

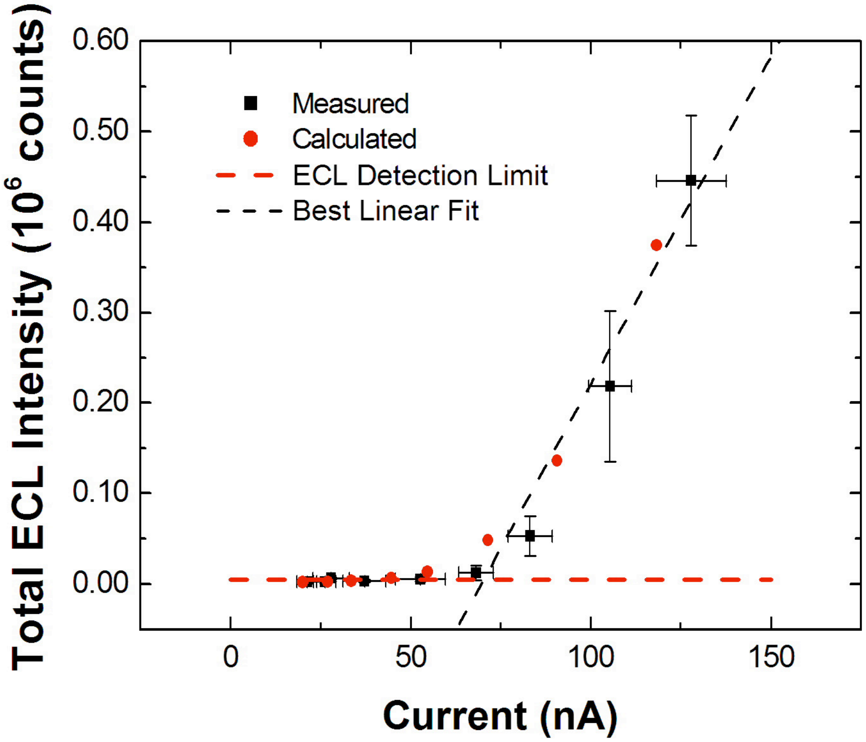

Figure 5.10. The black points represent the total ECL intensity for a split bipolar electrode as a function of the measured current. The measured values represent the average of four independently prepared devices. The dashed red line is the ECL detection limit calculated from the measured value of the background noise plus three times the standard deviation on this measurement. The black dashed line is the best fit for the linear part of the curve.

likely be useful as a reporter for quantitative sensing applications. The reporting sensitivity, that is the amount of light emitted per unit of current flowing through the electrode, is easily calculated from the slope of the linear segment in Figure 5.10 (dashed black line). Under the conditions used in our experiments, the reporting sensitivity is about 7200 counts/nA.

From an analytical perspective, the threshold current governs the limit of detection for a species that is being reduced at the cathodic pole. Indeed, the reduction of an analyte must be able to produce a current that is higher than the threshold value before ECL emission will reveal its presence. The lowest current density that can be indirectly detected through ECL reporting is about 32 $\mu A/cm^2$. This value was determined from the threshold current required for detection of ECL and the surface area of the bipolar electrode.

The presence of the threshold current means that faradaic reactions that do not produce detectable light occur at the bipolar electrode at low overpotential. It is well established that the principal pathway for ECL emission at high concentrations of $Ru(bpy)_3^{2+}$ (>500 μM) involves the catalytic, homogeneous cross-reaction between

$Ru(bpy)_3^{3+}$ and TPrA. However, a separate pathway involving direct TPrA oxidation at the electrode surface also occurs competitively at pH > 6.[23, 43, 44] Both pathways require direct oxidation of $Ru(bpy)_3^{2+}$ at the electrode surface, but the direct oxidation of TPrA occurs at a lower potential than $Ru(bpy)_3^{2+}$ oxidation on Au electrodes. The important point is that under the conditions used in our experiments TPrA oxidizes before $Ru(bpy)_3^{2+}$, but direct oxidation of $Ru(bpy)_3^{2+}$ is required to detect ECL. These considerations correlate with our experimental finding that current is observed at the bipolar electrode at potentials where no ECL is detected. That is, this pre-ECL current may be attributable to the oxidation of TPrA prior to the onset of $Ru(bpy)_3^{2+}$ oxidation.[23]

In addition to the representation shown in Figure 5.10, the threshold faradaic current can also be visualized by overlaying the linear ECL and current density profiles (Figure 5.11). For example, at E_{tot} = 23.0 V a region of the electrode, ranging from 0.86 to 0.96 mm, is observed where there is significant faradaic current but no detectable ECL emission. Significantly, the difference in overpotential between the onset of faradaic current and the onset of ECL is similar to that usually observed for the oxidation of

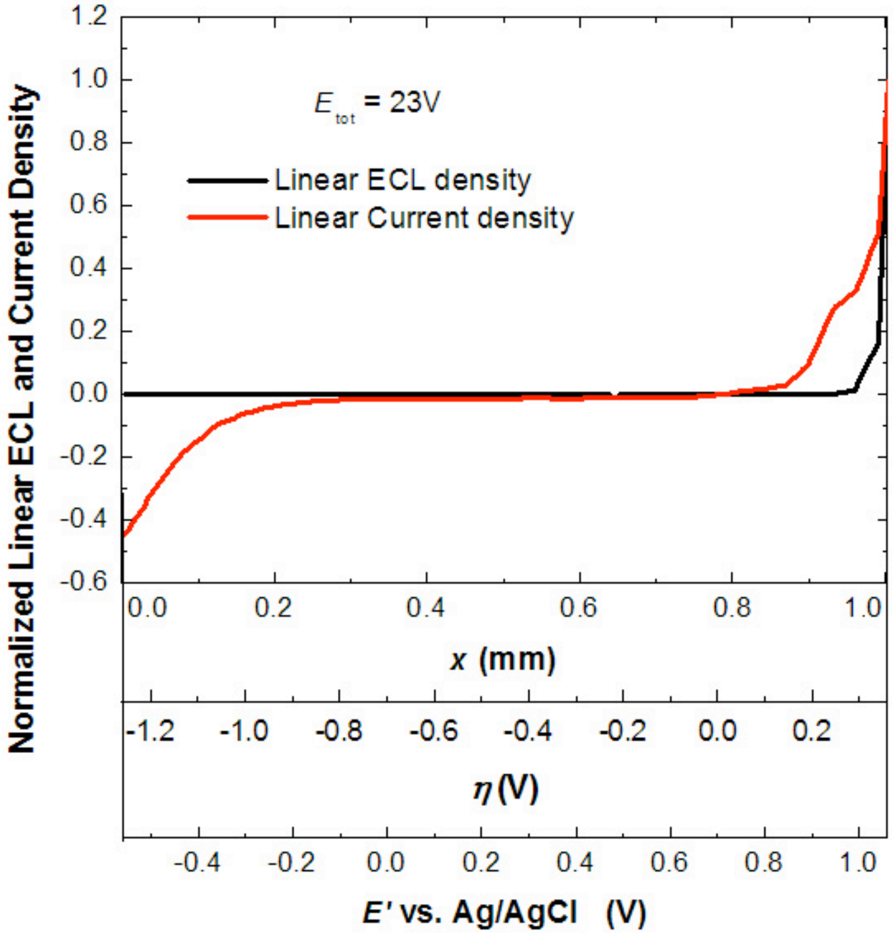

Figure 5.11. Normalized calculated linear ECL and current densities for E_{tot} = 23.0 V as a function of distance along the bipolar electrode, the overpotential, and the potential versus a Ag/AgCl reference electrode.

TPrA and $Ru(bpy)_3^{2+}$ [23, 44](here, about 0.85 and 0.97 V vs. Ag/AgCl, respectively, as noted on the potential scale of Figure 5.11). An alternative perspective is that the anodic overpotential (η scale in Figure 5.11) must attain a value of at least 0.3 V before ECL is detected. This means that the lowest analyte concentration that will result in light emission must be sufficiently large that the equilibrium potential taken by the bipolar electrode is high enough for at least 0.3 V to be dropped between x_0 and the far right end of the electrode l_{elec} (Scheme 5.2).

One way to increase the overpotentials on the anodic pole for a given driving voltage is to change the geometry of the electrode. Indeed, if the electrode area is reduced on its right side, more overpotential will be required to balance the cathodic processes at the other end. In other words, x_0 is shifted closer to the cathodic pole. This shift of x_0 forces the anodic overpotential, η_a, to increase. Therefore, the emission of light will occur for a lower bipolar current. Experimental evidence of this phenomenon has already been reported using a T shape electrode.[19]

5.5 Summary and Conclusions

This chapter provided a theoretical framework for understanding analytical applications of bipolar electrodes and bipolar electrode arrays. Experimental confirmation of this framework has also been provided. The key findings are as follows. First, a semi-empirical prediction of current flow through a bipolar electrode has been rigorously described. These results were successfully correlated to direct measurements of the total current for a split electrode system that mimics the behavior of a bipolar electrode. Second, a similar approach was used to calculate the ECL emission profile along a bipolar electrode, and these predictions were confirmed experimentally. Third, ECL emission was related to the total amount of current flowing through the bipolar electrode and some conclusions concerning their relevance to chemical analysis were described.

Our attention is now focused on using the information reported here to fabricating large-scale bipolar arrays and to evaluating them for chemical sensing applications. Additionally, we are learning how to improve the sensitivity and limit of detection for ECL reporting from bipolar electrodes by manipulating the geometry of the cell and electrodes, and by introducing additives to the buffer solution to lower overpotentials for ECL emission.

Table 5.2. Major Symbols

Symbol	**Meaning**	**Unit**
$\eta_{(x)}$	Difference of potential between the electrode and the solution at position *x*	V
η_{a}	Maximum anodic overpotential	V
η_{c}	Maximum cathodic overpotential	V
ΔE_{elec}	Potential difference between two ends of the bipolar electrode	V
E_{a}	Most negative solution potential over the bipolar electrode	V
E_{c}	Most positive solution potential over the bipolar electrode	V
E_{elec}	Equilibrium potential of the bipolar electrode	V
$E_{l_{\mathrm{elec}}/2}$	Potential of the solution at the halfway along the channel	V
E_{zcd}	Potential of zero net current density	V
E_{tot}	Applied potential difference between two driving electrodes	V

E_{step}	Potential of the working electrode in the three electrode cell potentiostep experiment	V
i_{a}	Anodic current	A
i_{c}	Cathodic current	A
I_{ECL}	ECL emission density	counts/cm^2.s
j	Current density	A/cm^2
$j \bullet w$	Linear current density	A/cm
l_{channel}	Length of the microchannel	mm
l_{elec}	Length of the bipolar electrode	mm
P_{a}	Power delivered at the anodic pole	A.V/cm
P_{c}	Power delivered at the cathodic pole	A.V/cm
V_0	Electric field	V/cm
w	Width of the bipolar electrode	mm
x	Position on a bipolar electrode	mm
x_0	The position on the bipolar electrode where the potential of the electrode and solution are equal	mm

Chapter 6: A Sensing Platform Based on Electrodissolution of a Ag Bipolar Electrode

6.1 Synopsis

In this chapter we report a new type of sensing platform that is based on electrodissolution of a metallic bipolar electrode (BPE). When target DNA binds to a capture probe at the cathodic pole of the BPE, it triggers the oxidation and dissolution of Ag metal present at the anodic pole. The loss of Ag is easily detectable with the naked eye or a magnifying glass and provides a permanent record of the electrochemical history of the electrode. More importantly, the decrease in the length of the BPE can be directly correlated to the number of electrons passing though the BPE and hence the sensing reaction at the cathode.

6.2 Introduction

In this chapter we report a new type of sensing platform that is based on electrodissolution of a metallic bipolar electrode (BPE). The concept is illustrated in Scheme 6.1a: Hybridization of horseradish peroxidase (HRP)

Scheme 6.1

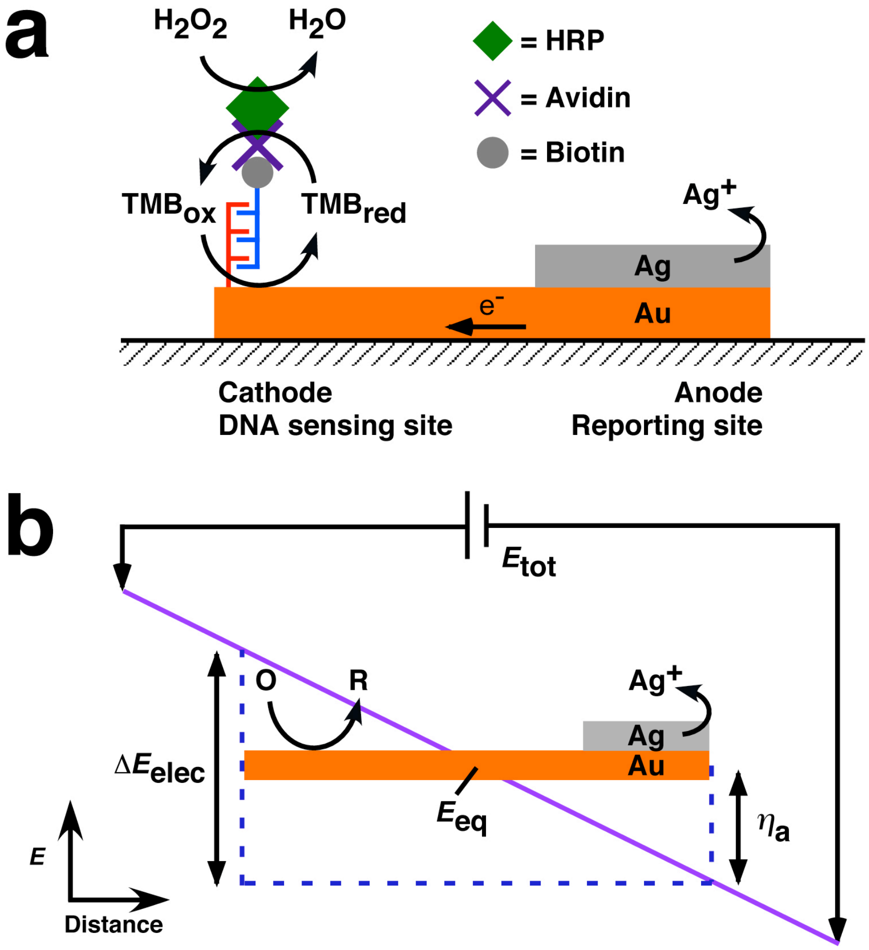
a
H2O2
H2O
= HRP
= Avidin
= Biotin
TMBox
TMBred
Ag+
Ag
Au
e-
Cathode
DNA sensing site
Anode
Reporting site
b
Etot
O
R
Ag+
Ag
Au
ΔEelec
Eeq
ηa
E
Distance

labeled DNA activates the oxidation of tetramethylbenzidine (TMB). When an electric field is applied, the enzyme generated oxidized form of TMB can be reduced at the cathodic end of a BPE simultaneously with the oxidation and dissolution of Ag metal present at the anodic end. The loss of Ag is easily detectable with the naked eye or a magnifying glass. More importantly, the decrease in the length of BPE, as it begins to dissolve, can be directly correlated to the number of electrons passing though the BPE and hence to the DNA binding process at the cathode. Important properties of this device include the following: (1) Ag dissolution provides a physical record of the sensing event; (2) because no direct connection to the BPEs is required, very large arrays of electrodes can be managed simultaneously with no additional instrumentation or device fabrication required;[45] (3) the only instrumentation required for running this device is a power supply or 12 V battery; and most importantly (4) because the Ag layer can have any desired thickness, this device has the potential to be highly sensitive and have a very low limit of detection.

The theory of bipolar electrochemistry has been described in several recent publications,[2, 3, 28] and a number of interesting applications have been reported.[10, 19, 27, 45, 46] The specific operating principles used in this study are illustrated in Scheme 6.1b. When a driving voltage (E_{tot}) is applied across the two ends of a microchannel, a linear potential drop develops in the buffer solution filling the channel. This will cause the potential of the BPE to float to an equilibrium value (E_{eq}) relative to the solution. When the solution potential difference (ΔE_{elec}) between the two ends of the BPE is larger than the cell potential for a pair of faradaic reactions, electrochemical reactions will occur at the cathodic and anodic poles of the BPE. Importantly, the reduction and oxidation reactions are exactly correlated; that is, the rate of one is identical to the rate of the other. Accordingly, a sensing event, like DNA hybridization (Scheme 6.1a), triggers an amount of Ag dissolution that is directly correlated to the triggering event.

6.3 Experimental

Chemicals and materials Gold-coated slides (EMF, Ithaca, NY) were used to fabricate the bipolar electrodes (BPEs). A silicone sheet (JTR-S-0.5, Grace bio-labs, Bend, OR) was used as the gasket material to form the microchannel. Tris(2-carboxyethyl)phosphine (TCEP) was obtained from Thermo Fisher Scientific.

All DNA oligonucleotides were synthesized and purified (HPLC) by Integrated DNA Technologies (Coralville, IA) and used without further purification. The sequences and modifications are as follows: capture probe, (5′-S-$(CH_2)_6$-CAA GAC AGC ACT ACA TCC CA-3′); target (5′-biotin-TGG GAT GTA GTG CTG TCT TG-3′). The capture probe DNA was dispensed in 0.20 M phosphate buffer (pH 6.9) containing 5.0 mM TCEP for reduction of the disulfide bond. Target DNA was diluted into PerfectHyb Plus hybridization buffer, (Sigma, henceforth referred to as hybridization buffer) and then dispensed onto the device.

Horseradish peroxidase (HRP) conjugated with avidin was obtained from Thermo Fisher Scientific (Rockford, IL). It was dissolved in enzyme buffer: 50.0 mM TRIS base, 0.5 M Na_2SO_4, 1 mM $MgSO_4$, 0.1% (v/v) Tween-20, and 1 mg/mL BSA.

A microscope (Nikon AZ 100, Nikon Co., Tokyo, Japan) equipped with a CCD camera (Cascade, Photometrics Ltd., Tucson, AZ) was used to obtain the optical micrographs. Micrographs were proceed using V++ Precision Digital Imaging software (Digital Optics, Auckland, New Zealand).

An electrometer (Electrometer 6517B, Keithley Instruments, Cleveland, OH) was used to measure the current.

Fabrication of bipolar electrodes and microfluidic devices The BPEs were fabricated by photolithography. Gold-coated slides (100 nm Au and 5 nm Cr on glass) were first cleaned with piranha solution. (Warning: piranha solution is a strong oxidant and reacts violently with organic materials. It should be handled with extreme care and all work should be performed under a fume hood and with protective gear). A layer of positive photoresist (~15 μm thick, AZ P4620, AZ Electronic Materials, Branchburg, NJ) was then spin-coated onto the Ag slide. Next, the photoresist layer was patterned (using a mask aligner) by illuminating the photoresist with UV light through a positive mask containing the BPE design. These patterns were then transferred to the Au slide after developing the photoresist and etching the Au layer using 5% I_2 plus 10% KI (v/v) for 2 min and the Cr adhesion layer using 9% $Ce(NH_4)_2(NO_3)$ plus 6% $HClO_4$ (v/v) for 30 s. The remaining photoresist was removed with acetone. After cleaning the patterned slide with piranha again, Cr and Ag were deposited on the anodic end of the BPE by lift-off.

The microchannel was formed by placing a 0.5 mm-thick silicone gasket, having the dimensions of the microchannel (12.0 mm long, 2.5 mm wide) cut into it, between a PDMS block and the glass slide supporting the BPEs. Two 3 mm-diameter reservoirs were punched into the PDMS block for filling the channel and to accommodate the driving electrodes.

DNA Modification of the BPE In the DNA sensing experiment, the Ag portion of the BPE was first covered with a layer of photoresist to protect the Ag layer from damage during the modification procedures. Specifically, we observed that the Ag layer could be damaged by the plasma cleaning or exposure to the hybridization buffer.

The BPEs were then cleaned in an air plasma (PDC-32G, Harrick Plasma, Ithaca, NY) for 30 s. Next, the middle BPE was modified with DNA by isolating it within a PDMS microchannel and flowing through a thiol-modified DNA solution (1.0 μM). After 1 h, the microchannel was removed and the BPEs were rinsed with water for 15 s. 50.00 μL of aqueous 1.0 mM 6-mercaptohexanol was placed on the surface of all 3 BPEs for 2 h to fill vacancies within the DNA monolayer (middle electrode) and prevent nonspecific adsorption (the other two electrodes). The electrodes were then rinsed with water again for 15 s prior to hybridization in a 90% humidity chamber with 30.00 µL of 1.0 µM biotin-modified target DNA in 0.5x hybridization buffer for 1 h. Next, the electrodes were rinsed with 0.10 M PBS for 15 s. 30.00 µL of 1% BSA in enzyme buffer was placed on the BPE surface for 15 min to prevent nonspecific adsorption of the HRP-avidin conjugate. 30.0 µL of 3 µg/mL HRP-avidin was placed on the electrode surface for 30 min to ensure binding to the biotinylated target DNA. Finally, the electrodes were rinsed for 30 s using 0.10 M PBS.

Following DNA modification and hybridization, the photoresist was selectively removed from the Ag-coated ends of the BPEs by isolating both the cathodic and anodic poles in parallel microchannels. Acetone was passed through the channel covering the anodic pole to dissolve the photoresist. The channel covering the cathodic pole remained empty, and was used only to prevent the PDMS from contacting the Au surface.

6.4 Results and Discussion

Part a of Figure 6.1 shows two types of BPEs housed inside a microchannel (1.2 cm long x 2.5 mm wide X 0.5 mm high).[2] Both the continuous and split electrode

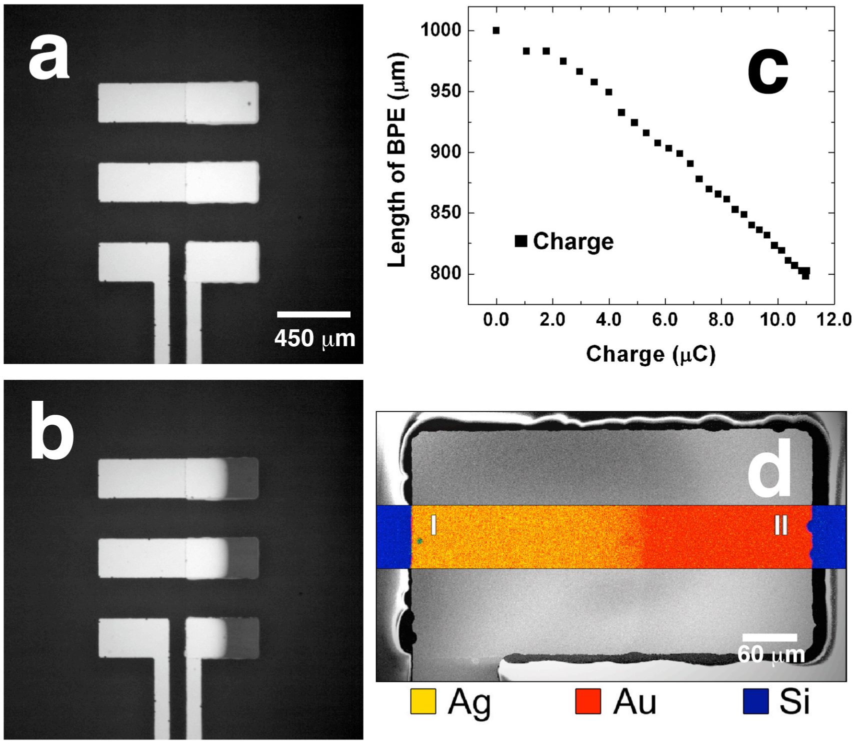

Figure 6.1. Optical micrographs of bipolar and split BPEs (a) before and (b) after application of E_{tot} = 12 V for 290 s. (c) Calibration plot showing the linear relationship between Ag film length and charge passed. (d) Electron micrograph of the anodic pole of the split BPE overlaid with an EDS element map.

configurations have an edge-to-edge length of 1.00 mm and are 0.25 mm wide. The BPEs were fabricated on glass by depositing 5 nm of Cr and 20 nm of Ag over 0.45 mm of the distal anodic pole of the BPE. The Cr layer enhances the optical contrast between the Ag and Au layers, which makes it easier to observe dissolution of Ag. The two halves (each 0.45 mm x 0.25 mm) of the split BPE are separated by 0.10 mm, and their inner edges are connected to an ammeter via contacts that extend out of the channel. We have previously demonstrated that a pair of split BPEs connected together with an ammeter is equivalent to a continuous bipolar electrode of the same overall length.[2] Two Ag/AgCl driving electrodes were placed in the reservoirs at either end of the microchannel, and an external field was applied via a power supply.

The microchannel housing the BPEs shown in Figure 6.1a was filled with 1.00 mM *p*-benzoquinone (a sacrificial oxidant) in 0.10 M acetate buffer at pH 5.5. When 12.0 V (E_{tot}) is applied to the driving electrodes, *p*-benzoquinone is reduced at the cathodic poles of the BPEs. This triggers oxidation of Ag at the anodic pole, which starts at the distal ends of the anodic poles and proceeds toward the center of the BPE. Figure 6.1b shows that after 290 s the lengths of the BPEs uniformly decreased to 0.797 ± 0.005 mm (Figure 6.1b).

The key observation that enables this BPE configuration to be used for chemical sensing is that Ag electrodissolution starts at the distal end of the anodic pole and proceeds inward toward the center. This finding is anticipated from our earlier studies,[2] which showed that the anodic overpotential (η_a, Scheme 6.1b) increases from the position of E_{eq} to the outer edge of the BPE (Scheme 6.1a). Because the overpotential is always highest at the outer edge of the electrode, dissolution preferentially occurs there. Electrodissolution of the BPE will eventually stop when the electrode length has decreased to a point where ΔE_{elec} (that is the electric field strength times the electrode length) is no longer high enough to drive oxidation of Ag and reduction of *p*-benzoquinone.[28]

Because it is possible to measure the current flowing through the split BPE, the visually determined shortening of the electrode can be directly correlated to total charge passed at any time during the experiment. Results representing this experiment are shown in Figure 6.1c. For example, after 290 s, 10.6 μC had been passed through the BPE. Taking into account the cross-sectional area of the

BPE and the density of Ag, this corresponds to a calculated decrease in the length of the electrode of 0.22 mm. This value corresponds closely to the measured reduction in length: 0.203 ± 0.005 mm (Figure 6.1b).

Figure 6.1d is an electron micrograph and element map of the anodic pole of the split BPE shown in Figure 6.1b taken after electrodissolution of Ag. The Ag, Au, and Si signals were recorded horizontally along the electrode and quantified at the indicated locations. For example, comparison of the element EDS spectra at spots I and II indicates that the Ag signal is reduced by 99%.

To demonstrate the biosensing function illustrated in Scheme 6.1a, the cathodic pole of the middle BPE shown in Figure 6.2a was modified with 20 nucleotide-long, thiol-modified capture DNA and the other two electrodes were modified with 6-mercaptohexanol. After immobilization, all three BPEs were exposed to 30.0 μL of 1.00 μM biotin-modified, complementary target DNA and subsequently to 30.0 μL of 3 μg/mL avidin-functionalized horseradish peroxidase (HRP). Under these conditions, hybridization of DNA should occur only on the middle BPE. The channel was then filled with 0.10 M acetate buffer (containing 1.6% (v/v) DMSO at pH 5.5) plus 0.42 mM tetramethylbenzidine (TMB) and 1.3 mM

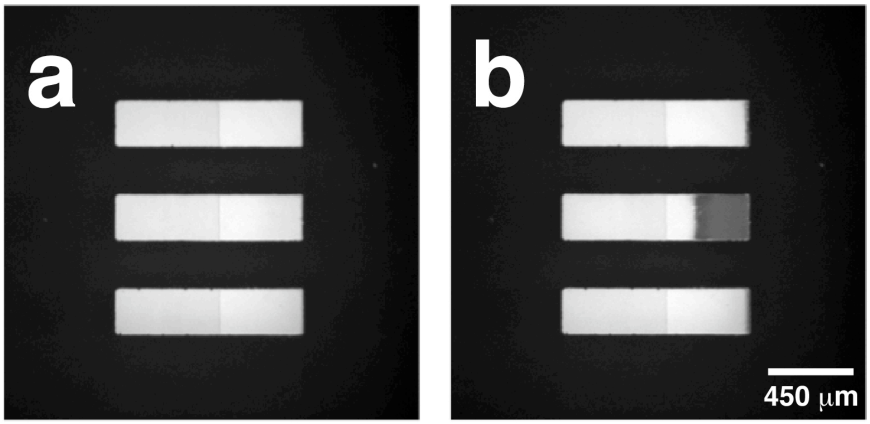

Figure 6.2. Optical micrographs of the DNA-sensing device (Scheme 1a) showing DNA-modified (middle) and thiol-modified (top and bottom) electrodes (a) before and (b) after E_{tot} = 12 V was applied for 90 s.

H_2O_2. HRP catalyzes the reduction of H_2O_2 to H_2O while simultaneously oxidizing the reduced form of TMB (TMB_{red}) to the oxidized form (TMB_{ox}).[16] If ΔE_{elec} is sufficiently high, then enzyme-generated TMB_{ox} can be reduced back to TMB_{red} at the cathodic pole of the BPE. This process triggers Ag oxidation at the anodic pole, which serves to signal DNA hybridization by visual inspection.

Figure 6.2b shows that when E_{tot} = 12.0 V, the length of the Ag on the middle BPE decreased by 0.29 mm after 90 s. The length of the unmodified electrodes did not change, indicating that DNA hybridization did not occur on the top and bottom BPEs.

Other BPE materials The bipolar electrodes used in the experiments discussed thus far are fabricated from gold and silver. However, these are not the only metals suitable for naked-eye BPE sensing. Any metal can be used on both anodic and cathodic ends of a BPE. The most important factor for picking a metal is the potential window required for the application.

Gold was used at the cathodic end of the bipolar electrode for the just-described DNA sensing experiment because of the simplicity of forming a DNA SAM. Thiol-modified DNA can easily be immobilized on gold via thiol-gold bond formation. The only disadvantage of using gold bipolar electrodes in a PDMS/glass base microfluidic channel is its small reduction potential window in the presence of dissolved oxygen. The ORR is kinetically favorable on gold surface, and therefore it is not suitable for detecting a reduction reaction occurring at a potential further negative than ~ -0.1 V vs. Ag/AgCl. This is because the current from the reduction of oxygen will interfere with the desired detection reaction.

In a typical three-electrode cell experiment, oxygen can be removed from the solution by sparging nitrogen or argon gas through the solution. However, PDMS is permeable to oxygen, and therefore it is nearly impossible to remove all oxygen.[47]

In a previous publication, we used an ITO BPE to detect benzyl viologen (BV^{2+}) in solution.[19] When BV^{2+} was present in the solution, ECL was emitted from the anodic end of the BPE. In a control experiment where BV^{2+} is absent, ECL was not observed. However, when the same experiment was carried out with a gold BPE, ECL was observed whether BV^{2+} was present or absent. We explain the observation of ECL in both cases to the nonspecific reduction of O_2; O_2 will reduce at a more positive potential than BV^{2+} on Au, and due to the PDMS permeability, will likely be present at high concentrations regardless of sample preparation. Thus, for true sensing chemistry, Au is an inappropriate material for aerobic environments.

In contrast, the reduction of O_2 is not kinetically favorable on ITO, and therefore ITO a wider potential window[48] for detecting a reduction reaction than gold does when oxygen is present in the solution. The experiment described below utilizes an ITO BPE.

Effect of halide ion The detection method reported here relies on dissolution of Ag. When Ag is being oxidized at the anodic BPE surface, it becomes Ag^+ and can form a precipitate with the halide ions present in the solution. In this section, the effect of silver halide salt will be discussed.

In this experiment, benzyl viologen dichloride salt was dissolved in 0.1 M phosphate buffer. The resulting solution contained 10.0 mM BV^{2+} and 20.0 mM Cl^-, and it was introduced into the microchannel of the BPE device shown in part a of Figure 6.3. The BPEs used in this experiment were made of Ag deposited on the anodic end of the ITO BPEs. Part b of Figure 6.3 shows an optical image of the device after E_{tot} = 15 V was applied for 100 s.

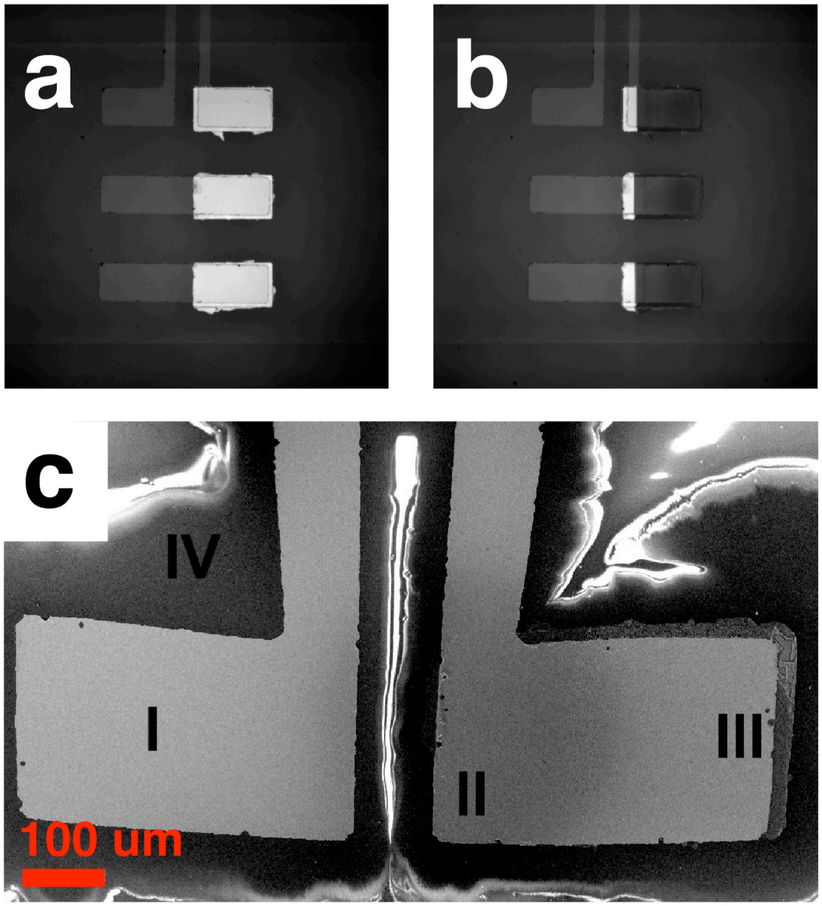

Figure 6.3. Optical micrograph of bipolar and split bipolar electrodes (a) before (b) after E_{tot} = 15 V applied for 100 s. (c) SEM image of the split BPE shown in part (b). The roman numbers indicate where EDS spots were taken. The relative elemental compositions are shown in Table 6.1.

Table 6.1. Elemental compositions of the BPE device after silver dissolution.

	ITO at cathode (spot I)	**Unoxidized Ag at anode (spot II)**	**Oxidized Ag at anode (spot III)**	**Glass (spot IV)**
Ag	-	5	3.5	-
Cl	-	0.1	2.5	-
Si	33	27	31	9
In	19	22	22	-
O	30	21	25	61
C	4.5	17.9	7	24
Al	10	7	9	4
Mg	1.5	-	Trace	Trace
Ca	2	Trace	Trace	Trace
Cr	Trace	Trace	Trace	Trace
Ti	Trace	Trace	Trace	Trace

The length of the BPE shortened to 0.63 mm. By using the current measured through the ammeter connected to the split BPE and the geometry of the BPE, the theoretical resulting length of the BPE should be 0.69 mm. This value is in reasonable agreement with the experimental determined value in the presence of halide ions in the solution.

EDS was used to quantify the elemental composition on different regions of the electrode surface (part c of Figure 6.3 and Table 6.1). The important values for this analysis are the silver and chlorine values at the oxidized and unoxidized regions, because they show where AgCl forms. At the unoxidized region, 5% Ag was detected along with other elements. Comparing to the oxidized region, 3.5% of Ag and 2.5% of Cl were detected. There was no detectable amount of Ag and Cl present on the cathodic pole of the BPE and glass surface.

This experiment suggests that once the Ag is oxidized, it forms AgCl with the Cl^- ion in the solution and then precipitates onto the electrode surface. When Ag oxidizes to Ag^+ and most of it reacts rapidly with aqueous Cl^- to yield a film of porous AgCl that itself fosters the formation of addition AgCl with continued oxidation. A fraction of the Ag^+ would migrate into solution while the majority remained on the electrode as AgCl. Although AgCl is all over the oxidized part of the BPE, it has no effect on the dissolution of Ag at the anodic pole when a sensing experiment is carried out. This observation is also supported by the current measurement experiment described above.

For the reduction of benzoquninone in the experiment described above (Figure 6.1), there was no halide ion present in the solution. Therefore, in this control experiment, the Ag signal in the oxidized region was reduced by 99% compared to the unoxidized region. In addition, based on the comparison of the theoretically estimated length of the BPEs and the experimentally obtained results, the presence of low concentration of halide ions in solution have no negative effect on the dissolution of silver.

6.5 Summary and Conclusions

In summary, we have shown that BPE dissolution can be used to provide a permanent record of a sensing/recognition event. This method provides a number of key advantages over our previously reported approach based on electrogenerated chemiluminescence signaling.

Specifically, the sensitivity and limit of detection of the method are simply controlled by the cross-sectional area of the Ag patch on the BPE. Moreover, no optical readout is required: just the naked eye or a magnifying glass provides sufficient resolution to determine the state of the sensor. In addition to these advantages, the many desirable attributes of BPE sensing are retained: very simple instrumentation and simultaneous control and readout of thousands[45] or perhaps millions of BPEs.

Chapter 7: Summary and Conclusion

This dissertation describes the development of wireless DNA microelectrochemical microarray sensors. Both theoretical and experimental frameworks on bipolar electrode sensing have been studied. Different BPE microarray sensing platforms are developed, and some fundamental principles about bipolar electrode sensing have also been investigated.

Chapter 3 described the development of a wireless ECL based bipolar electrode microarray. The BPEs were immobilized with capture probe DNA and the anode end of each electrode was configured to emit light (ECL) upon hybridization of complementary DNA labeled with electrocatalytic (oxygen reduction) Pt nanoparticles at the cathode. The important finding was that DNA could be selectively detected at an array of three electrodes. This chapter demonstrated that only two wires are needed to control multiple electrodes simultaneously.

Chapter 4 described how 1000 bipolar electrodes were controlled by only two wires and a simple power supply. The system was configured so that faradaic processes occurring at the cathode end of each electrode were correlated to light emission via ECL at the anode end. The state of each BPE could be read out simultaneously. The significant advance was that the electrode array was fabricated on a glass microscope slide and was operated in a simple electrochemical cell. This chapter also discussed the use of a robotic spotter to immobilize different DNA sequences at the cathodic end of each BPE on a microarray. This development allowed each BPE on a microarray to perform different sensing task.

Chapter 5 provided a detailed theoretical analysis of ECL reporting at bipolar electrodes. In addition, experiments were described that confirmed the theory. Split BPEs were designed to correlate the ECL intensity directly to the amount of current passing through the electrodes. The results indicated that the lowest current that could be indirectly detected through ECL reporting was about 32 $\mu A/cm^2$, which corresponded to a reporting sensitivity of about 7200 counts/nA in the present experimental system.

Chapter 6 discussed a new type of sensing platform that was based on electrodissolution of a metallic BPE. When target DNA bound to the capture probe at the cathodic pole of the BPE, it triggered the oxidation and dissolution of Ag metal present at the anodic pole. The loss of Ag was easily detectable with the naked eye or a magnifying glass and provided a permanent record of the electrochemical history of the electrode. More importantly, the decreased in the length of the BPE could be directly correlated to the number of electrons passing though the BPE and hence the sensing reaction at the cathode.

References

(1) Bard, A. J.; Faulkner, L. R. *Electrochemical Methods: Fundamentals and Applications*, 2nd ed.; J. Wiley & Sons, Inc.: New York, 2001.

(2) Mavré, F.; Chow, K.-F.; Sheridan, E.; Chang, B.-Y.; Crooks, J. A.; Crooks, R. M. A Theoretical and Experimental Framework for Understanding Electrogenerated Chemiluminescence (ECL) Emission at Bipolar Electrodes *Anal. Chem.* **2009**, *81*, 6218-6225.

(3) Fleischmann, M.; Ghoroghchian, J.; Rolison, D.; Pons, S. Electrochemical-Behavior of Dispersions of Spherical Ultramicroelectrodes *J. Phys. Chem.* **1986**, *90*, 6392-6400.

(4) Ghoroghchian, J.; Pons, S.; Fleischmann, M. Gas-Phase Electrochemistry on Dispersions of Microelectrodes *J. Electroanal. Chem.* **1991**, *317*, 101-108.

(5) Smotkin, E.; Bard, A. J.; Campion, A.; Fox, M. A.; Mallouk, T.; Webber, S. E.; White, J. M. Bipolar TiO_2/Pt Semiconductor Photoelectrodes and Multielectrode Arrays for Unassisted Photolytic Water Splitting *J. Phys. Chem.* **1986**, *90*, 4604-4607.

(6) Smotkin, E. S.; Cerveramarch, S.; Bard, A. J.; Campion, A.; Fox, M. A.; Mallouk, T.; Webber, S. E. Bipolar CdSe/CoS Semiconductor Photoelectrode Arrays for Unassisted Photolytic Water Splitting *J. Phys. Chem.* **1987**, *91*, 6-8.

(7) Cerveramarch, S.; Smotkin, E. S.; Bard, A. J.; Campion, A.; Fox, M. A.; Mallouk, T.; Webber, S. E.; White, J. M. Modeling of Bipolar Semiconductor Photoelectrode Arrays for Electrolytic Processes *J. Electrochem. Soc.* **1988**, *135*, 567-573.

(8) Bradley, J.-C.; Chen, H.-M.; Crawford, J.; Eckert, J.; Ernazarova, K.; Kurzeja, T.; Lin, M.; McGee, M.; Nadler, W.; Stephens, S. G. Creating Electrical Contacts Between Metal Particles Using Directed Electrochemical Growth *Nature* **1997**, *389*, 268-271.

(9) Wang, Y.; Hernandez, R. M.; Bartlett, D. J.; Bingham, J. M.; Kline, T. R.; Sen, A.; Mallouk, T. E. Bipolar Electrochemical Mechanism for the Propulsion of Catalytic Nanomotors in Hydrogen Peroxide Solutions *Langmuir* **2006**, *22*, 10451-10456.

(10) Ulrich, C.; Andersson, O.; Nyholm, L.; Björefors, F. Formation of molecular gradients on bipolar electrodes *Angew. Chem.-Int. Edit.* **2008**, *47*, 3034-3036.

(11) Ulrich, C.; Andersson, O.; Nyholm, L.; Björefors, F. Potential and Current Density Distributions at Electrodes Intended for Bipolar Patterning *Anal. Chem.* **2009**, *81*, 453-459.

(12) Warakulwit, C.; Nguyen, T.; Majimel, J.; Delville, M. H.; Lapeyre, V.; Garrigue, P.; Ravaine, V.; Limtrakul, J.; Kuhn, A. Dissymmetric Carbon Nanotubes by Bipolar Electrochemistry *Nano Lett.* **2008**, *8*, 500-504.

(13) Ramakrishnan, S.; Shannon, C. Display of Solid-State Materials Using Bipolar Electrochemistry *Langmuir* **2010**, *26*, 4602-4606.

(14) Sassolas, A.; Leca-Bouvier, B. D.; Blum, L. J. DNA Biosensors and Microarrays *Chem. Rev.* **2008**, *108*, 109-139.

(15) Polsky, R.; Gill, R.; Kaganovsky, L.; Willner, I. Nucleic Acid-Functionalized Pt Nanoparticles: Catalytic Labels for the Amplified Electrochemical Detection of Biomolecules *Anal. Chem.* **2006**, *78*, 2268-2271.

(16) Ghindilis, A. L.; Smith, M. W.; Schwarzkopf, K. R.; Roth, K. M.; Peyvan, K.; Munro, S. B.; Lodes, M. J.; Stöver, A. G.; Bernards, K.; Dill, K.; McShea, A. CombiMatrix oligonucleotide arrays: Genotyping and

gene expression assays employing electrochemical detection *Biosens. Bioelectron.* **2007**, *22*, 1853-1860.

(17) Xia, Y.; Rogers, J. A.; Paul, K. E.; Whitesides, G. M. Unconventional Methods for Fabricating and Patterning Nanostructures *Chem. Rev.* **1999**, *99*, 1823-1848.

(18) Williams, K. R.; Gupta, K.; Wasilik, M. Etch Rates for Micromachining Processing - Part II *J. Microelectromech. Syst.* **2003**, *12*, 761-778.

(19) Zhan, W.; Alvarez, J.; Crooks, R. M. Electrochemical Sensing in Microfluidic Systems Using Electrogenerated Chemiluminescence as a Photonic Reporter of Redox Reactions *J. Am. Chem. Soc.* **2002**, *124*, 13265-13270.

(20) Arora, A.; Eijkel, J. C. T.; Morf, W. E.; Manz, A. A Wireless Electrochemiluminescence Detector Applied to Direct and Indirect Detection for Electrophoresis on a Microfabricated Glass Device *Anal. Chem.* **2001**, *73*, 3282-3288.

(21) Leland, J. K.; Powell, M. J. Electrogenerated Chemiluminescence: An Oxidative-Reduction Type ECL Reaction Sequence Using Tripropyl Amine *J. Electrochem. Soc.* **1990**, *137*, 3127-3131.

(22) Bard, A. J. *Electrogenerated Chemiluminescence*; Marcel Dekker, Inc.: New York, 2004.

(23) Miao, W.; Choi, J.-P.; Bard, A. J. Electrogenerated Chemiluminescence 69: The Tris(2,2'-bipyridine)ruthenium(II), $(Ru(bpy)_3^{2+})$/Tri-n-propylamine (TPrA) System Revisited - A New Route Involving TPrA$^{\cdot+}$ Cation Radicals *J. Am. Chem. Soc.* **2002**, *124*, 14478-14485.

(24) Yang, J.; Lee, J. Y.; Too, H.-P. Size Effect in Thiol and Amine Binding to Small Pt Nanoparticles *Anal. Chim. Acta.* **2006**, *571*, 206-210.

(25) Steel, A. B.; Herne, T. M.; Tarlov, M. J. Electrochemical Quantitation of DNA Immobilized on Gold *Anal. Chem.* **1998**, *70*, 4670-4677.

(26) Xia, Y.; Whitesides, G. M. Soft Lithography *Angew. Chem. Int. Ed.* **1998**, *37*, 550-575.

(27) Chow, K.-F.; Mavré, F.; Crooks, R. M. Wireless Electrochemical DNA Microarray Sensor *J. Am. Chem. Soc.* **2008**, *130*, 7544-7545.

(28) Duval, J. F. L.; Kleijn, J. M.; van Leeuwen, H. P. Bipolar Electrode Behaviour of the Aluminium Surface in a Lateral Electric Field *J. Electroanal. Chem.* **2001**, *505*, 1-11.

(29) Duval, J. F. L.; van Leeuwen, H. P.; Cecilia, J.; Galceran, J. Rigorous analysis of reversible faradaic

depolarization processes in the electrokinetics of the metal/electrolyte solution interface *J. Phys. Chem. B* **2003**, *107*, 6782-6800.

(30) Ulrich, C.; Andersson, O.; Nyholm, L.; Björefors, F. Potential and Current Density Distributions at Electrodes Intended for Bipolar Patterning *Anal. Chem.* **2009**, *81*, 453-459.

(31) Piruska, A.; Branagan, S.; Cropek, D. M.; Sweedler, J. V.; Bohn, P. W. Electrokinetically Driven Fluidic Transport in Integrated Three-Dimensional Microfluidic Devices Incorporating Gold-Coated Nanocapillary Array Membranes *Lab Chip* **2008**, *8*, 1625-1631.

(32) Duval, J. F. L.; Minor, M.; Cecilia, J.; van Leeuwen, H. P. Coupling of Lateral Electric Field and Transversal Faradaic Processes at the Conductor/Electrolyte Solution Interface *J. Phys. Chem. B* **2003**, *107*, 4143-4155.

(33) LaFratta, C. N.; Walt, D. R. Very High Density Sensing Arrays *Chem. Rev.* **2008**, *108*, 614-637.

(34) Zhan, W.; Alvarez, J.; Crooks, R. M. A Two-Channel Microfluidic Sensor that Uses Anodic Electrogenerated Chemiluminescence as a Photonic Reporter of Cathodic Redox Reactions *Anal. Chem.* **2003**, *75*, 313-318.

(35) Klett, O.; Nyholm, L. Separation High Voltage Field Driven On-Chip Amperometric Detection in Capillary Electrophoresis *Anal. Chem.* **2003**, *75*, 1245-1250.

(36) Ordeig, O.; Godino, N.; del Campo, J.; Muñoz, F. X.; Nikolajeff, F.; Nyholm, L. On-Chip Electric Field Driven Electrochemical Detection Using a Poly(dimethylsiloxane) Microchannel with Gold Microband Electrodes *Anal. Chem.* **2008**, *80*, 3622-3632.

(37) Zhan, W.; Alvarez, J.; Crooks, R. M. A Two-Channel Microfluidic Sensor that Uses Anodic Electrogenerated Chemiluminescence as a Photonic Reporter of Cathodic Redox Reactions *Anal. Chem.* **2003**, *75*, 313-318.

(38) Zhan, W.; Alvarez, J.; Sun, L.; Crooks, R. M. A Multichannel Microfluidic Sensor that Detects Anodic Redox Reactions Indirectly Using Anodic Electrogenerated Chemiluminescence *Anal. Chem.* **2003**, *75*, 1233-1238.

(39) Zhan, W.; Crooks, R. M. Microelectrochemical Logic Circuits *J. Am. Chem. Soc.* **2003**, *125*, 9934-9935.

(40) Duval, J. F. L.; Sorrenti, E.; Waldvogel, Y.; Görner, T.; De Donato, P. On the Use of Electrokinetic Phenomena of the Second Kind for Probing Electrode

Kinetic Properties of Modified Electron-Conducting Surface *Phys. Chem. Chem. Phys.* **2007**, *9*, 1713-1729.

(41) Zhan, W.; Alvarez, J.; Sun, L.; Crooks, R. M. A Multichannel Microfluidic Sensor that Detects Anodic Redox Reactions Indirectly Using Anodic Electrogenerated Chemiluminescence *Anal. Chem.* **2003**, *75*, 1233-1238.

(42) Noffsinger, J. B.; Danielson, N. D. Generation of Chemiluminescence Upon Reaction of Aliphatic Amines with Tris(2,2'-bipyridine)ruthenium(III) *Anal. Chem.* **1987**, *59*, 865-868.

(43) Gross, E. M.; Pastore, P.; Wightman, R. M. High-Frequency Electrochemiluminescent Investigation of the Reaction Pathway between Tris(2,2'-bipyridyl)ruthenium(II) and Tripropylamine Using Carbon Fiber Microelectrodes *J. Phys. Chem. B* **2001**, *105*, 8732-8738.

(44) Kanoufi, F.; Zu, Y.; Bard, A. J. Homogeneous Oxidation of Trialkylamines by Metal Complexes and Its Impact on Electrogenerated Chemiluminescence in the Trialkylamine/$Ru(bpy)_3^{2+}$ System *J. Phys. Chem. B* **2000**, *105*, 210-216.

(45) Chow, K.-F.; Mavré, F.; Crooks, J. A.; Chang, B.-Y.; Crooks, R. M. A Large-Scale, Wireless Electrochemical Bipolar Electrode Microarray *J. Am. Chem. Soc.* **2009**, *131*, 8364-8365.

(46) Laws, D. R.; Hlushkou, D.; Perdue, R. K.; Tallarek, U.; Crooks, R. M. Bipolar Electrode Focusing: Simultaneous Concentration Enrichment and Separation in a Microfluidic Channel Containing a Bipolar Electrode *Anal. Chem.* **2009**, *81*, 8923-8929.

(47) Mukhopadhyay, R. When PDMS isn't the Best *Anal. Chem.* **2007**, *79*, 3248-3253.

(48) Crespilho, F. N.; Nart, F. C.; Oliverira, O. N.; Brett, C. M. A. Oxygen Reduction and Diffusion in Electroactive Nanostructured Membranes (ENM) Using a layer-by-layer Dendrimer-gold Nanoparticle Approach *Electrochim. Acta* **2007**, *52*, 4649-4653.

Vita

Kwok-Fan Chow received his Bachelor of Science and Master of Science degrees from St. John’s University, NY in 2003 and 2005. He is expected to receive his doctoral degree in Chemistry under the guidance of Professor Richard M. Crooks from The University of Texas at Austin in August 2010.

Permanent address: 53-22 37th Road, Woodside, NY 11377
This dissertation was typed by Kwok-Fan Chow.